Design and Operation Principles of a Wave-Controlled Reconfigurable Intelligent Surface

GAL BEN-ITZHAK (Graduate Student Member, IEEE),
MIGUEL SAAVEDRA-MELO (Graduate Student Member, IEEE),
BENJAMIN BRADSHAW (Graduate Student Member, IEEE), ENDER AYANOGLU (Fellow, IEEE),
FILIPPO CAPOLINO (Fellow, IEEE), AND A. LEE SWINDLEHURST (Fellow, IEEE)

Center for Pervasive Communications and Computing, Department of Electrical Engineering and Computer Science,
University of California at Irvine, Irvine, CA 92697, USA

CORRESPONDING AUTHOR: E. AYANOGLU (e-mail: ayanoglu@uci.edu)

ABSTRACT A Reconfigurable Intelligent Surface (RIS) consists of many small reflective elements whose reflection properties can be adjusted to change the wireless propagation environment. Envisioned implementations require that each RIS element be connected to a controller, and as the number of RIS elements on a surface may be on the order of hundreds or more, the number of required electrical connectors creates a difficult wiring problem. A potential solution to this problem was previously proposed by the authors in which "biasing transmission lines" carrying standing waves are sampled at each RIS location to produce the desired bias voltage for each RIS element. This paper presents models for the RIS elements that account for mutual coupling and realistic varactor characteristics, as well as circuit models for sampling the transmission line to generate the RIS control signals. The paper investigates two techniques for conversion of the transmission line standing wave voltage to the varactor bias voltage, namely an envelope detector and a sample-and-hold circuit. The paper also develops a modal decomposition approach for generating standing waves that are able to generate beams and nulls in the resulting RIS radiation pattern that maximize either the Signal-to-Noise Ratio (SNR) or the Signal-to-Leakage-plus-Noise Ratio (SLNR). The paper provides five algorithms, two for the case of the envelope detector, one for the sample-and-hold circuit, one for pursuing the global minimum for both circuits, and one for simultaneous beam and null steering. Extensive simulation results show that while the envelope detector is simpler to implement, the sample-and-hold circuit has substantially better performance and runs in substantially less time. In addition, the wave-controlled RIS is able to generate strong beams and deep nulls in desired directions. This is in contrast with the case of arbitrary control of each varactor element and idealized RIS models.

INDEX TERMS Spatial Fourier series, envelope detection, sample-and-hold, least squares (LS), simulated annealing (SA).

I. INTRODUCTION

RECONFIGURABLE Intelligent Surface (RIS) technology provides controllable degrees-of-freedom (DoFs) for shaping the wireless radio-frequency (RF) channel in advantageous ways, for example by steering signals around blockages, providing beamforming gain to enhance signal-to-noise ratio (SNR) and reduce interference, and improving the overall quality-of-service (QoS) enjoyed by network users [1]. An RIS is populated by a typically large number of essentially passive (i.e., gainless) elements such as metallic patches whose reflective properties can be externally controlled. For an RIS with R rows and M elements per row, the total number of elements is defined as $M' = M \times R$. In common implementations, the reconfigurability is achieved by varying the biasing voltage across a varactor or the current through a p-i-n diode present in each element, which in

turn produces variations in the input impedance seen by impinging RF energy. When properly designed, the electrical control can tune the reflection phase of each element in a particular frequency band to nearly any value between $-\pi$ and π. Some designs also provide tunability of the reflection amplitude to values between 0 and 1 (due to the element's passivity), although in many cases it is common to maintain the amplitude as close to unity as possible.

At millimeter wave or terahertz frequencies, an RIS can be designed with hundreds or potentially thousands of elements in a relatively small form factor, enabling large beamforming gains and narrow reconfigurable pencil-like beams. While having such high gains and directivity is advantageous, it comes with certain implementational challenges. First, because most RIS designs do not include active receivers, they must be controlled by an external device such as an access point or basestation (BS). This means that the wireless channels to/from an M'-element RIS must be estimated remotely at the BS, which can lead to an M'-fold increase in the pilot overhead unless certain assumptions are made about the propagation environment, such as the presence of only sparse propagation paths (reasonable at high frequencies) [2]. Second, once the channel is estimated, the BS must determine the RIS configuration. This typically requires a complicated non-convex optimization over more than M' variables. Then the BS must transmit the optimal configuration composed of M' complex values to the RIS to control its behavior. Clearly, a large value for M' will in turn create a large signaling overhead. This overhead is often manageable since the RIS need only be updated at the channel coherence rate. However, techniques have nevertheless been proposed to compress the required amount of information flow using, for example, entropy coding [3] or by approximating the RIS phase vector using a low-rank tensor [4]. A third more difficult challenge arising from large RIS with many elements is the apparent need for M' wired connections to supply the required voltages or currents to all RIS elements. This requires an intricate design with potentially thousands of individual signal pathways throughout the device. Addressing this design issue has received considerably less attention, with some proposals suggesting the use of light-based controls. Towards that end, [5], [6], [7] created digital control commands using light-sensitive photodiodes. A scanning laser beam could potentially achieve this type of control, or the entire RIS could be illuminated with a single image where each RIS element receives a particular light intensity to achieve the desired control. Scanning has the limitation of speed and reach, whereas the image approach can be problematic due to weather conditions such as rain. Image resolution could also be a problem if the image source is far from the RIS.

To overcome these limitations, in this paper we propose an alternative technique that uses a *single* electric connection for each row of M unit cells, as shown in Fig. 1, resulting in a reduced-dimension method for controlling the RIS element behavior that leads to both a simpler
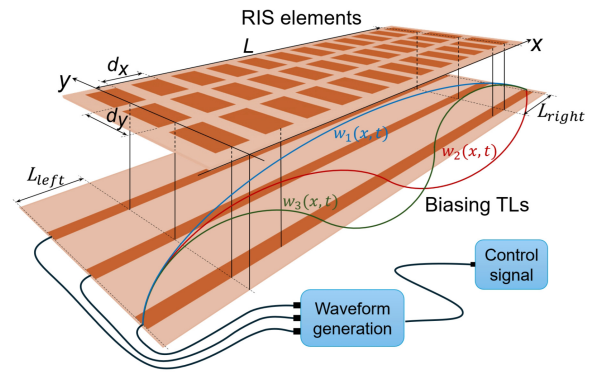
FIGURE 1. Wave-controlled RIS made of two physical layers. Top layer: M RIS elements in each row along x; each element is connected to a varactor diode. Bottom layer: N standing waves along the biasing transmission lines (TLs) to create the biasing voltages when sampled at each RIS element. Each row is controlled only by the connection at the left where N frequencies are injected by a waveform generator.

hardware implementation and a lower signaling overhead. Furthermore, we also provide an electromagnetic model to estimate analytically the reflection coefficient that accounts for mutual couplings and losses in the materials and includes a simple SPICE[1]-based model of a commercially available varactor.

II. ASSUMPTIONS AND NOTATION

We assume that each row (or column) of the RIS has M metallic patches connected with vertical vias to a waveguide (located at a lower level). This waveguide is excited in such a way to introduce N standing waves from which the biasing voltage for each element in the row can be induced [8]. As shown in Fig. 1, the standing waves are assumed to be parameterized by $N \ll M$ harmonic modes, whose coefficients form the control information that defines the RIS response.

A large reduction in degrees of freedom is foreseen for RIS that have a large number M of elements, for example on the order of hundreds or even thousands. To configure our wave-controlled RIS response, the BS only needs to perform an optimization over a much smaller number N of parameters, and thus the amount of data transmitted to the RIS can be reduced by a fraction of order $O(N/M)$ compared to what would normally be required for a standard RIS implementation. Alternatively, for the same control channel bandwidth, one could increase the quality (i.e., resolution) of the control information that is transmitted. For example, if for a conventional RIS the control signal for each of the M elements is transmitted using B bits of information, then for the same control channel bandwidth, one could transmit the N mode coefficients for the wave-controlled RIS with $BM/N > B$ bits of resolution each, which would result in increased control signal fidelity. The gains in reduced control overhead or increased control precision depend on whether the N modal coefficients are from the first N harmonics (the simplest case), or if they are selected (for example) as the N

---

[1]SPICE: Simulation Program with Integrated Circuit Emphasis.

largest among all the harmonics. In the latter case, additional information would have to be sent to indicate which modes are to be activated. An additional advantage of using the wave-controlled architecture is that the need for dense wiring and signal paths that would be required in a conventional RIS to physically connect to and control every RIS element is avoided, while still guaranteeing a large degree of control of the RIS. This offers a substantial reduction in the required hardware and implementation complexity that is particularly important at millimeter wave frequencies and higher where the physical space is limited.

We note here that the proposed architecture is different from that for so-called Dynamic Metasurface Antennas (DMAs) [9], [10], which also employ waveguides along the rows or columns of the metasurface to connect to the individual elements. However, in a DMA, the waves entering the surface at each element combine together and propagate along the waveguide before being sampled for processing. This allows for an active implementation with (for example) signal amplification, but the beamforming must take into account the inherent analog combining that occurs in the waveguide. The operation of our proposed design is more akin to a conventional RIS, the key difference being how the control signals for each RIS element are generated.

The procedure for channel estimation using our wave-controlled RIS is essentially the same as that for any other RIS. For example, during an uplink training phase, the RIS would cycle through a series of preset configurations that would provide sufficient information in order for the basestation (BS) to estimate the cascaded user-RIS-BS channel. In general, the RIS must be able to be configured into at least M unique configurations to provide the BS with sufficient independent observations of the channel to identify the channel components. Even if the value of each of the N modes is quantized to 2-3 bits in the control channel, there would still be as many as 4^N to 8^N different RIS configurations, which will be more than sufficient for reasonable values of N and M.

To describe the performance of our proposed wave-controlled approach, we first provide a detailed model for an RIS design based on varactor diode control, and verify the accuracy of the model using full-wave electromagnetic simulations. The model accounts for mutual coupling among the RIS elements. It also incorporates realistic non-ideal behavior due to losses in the metallic patches, in the dielectric substrate, and in the varactor diodes, leading to realistic voltage- and frequency-dependent variations in the RIS element reflection coefficient amplitudes and phases [11]. We also discuss methods to interface the waveguide control with the proposed RIS unit cells. We will present several numerical examples involving a reflective metasurface implementation to compare three different ways to control the RIS, namely: *i) Ideal Phase* – The reflection phases of the elements are perfectly tuned; *ii) Arbitrary Voltage Bias* – Each varactor is biased using an arbitrary voltage to create the reflection magnitude and phase

based on the analytical model of the RIS elements; *iii) Wave-Controlled Bias* – The standing waves are used to control the varactors and reflection coefficients. Since our model and RIS implementations are dramatically different from what is assumed in the literature, we compare our performance against what is achievable with an idealized RIS model. Although the optimizations required for this simplified conventional model do not take into account realistic physical limitations such as RF coupling, non-ideal gain responses, and limited phase responses, our waveguide-controlled approach still achieves performance close to that for the idealized model. The results demonstrate the ability of the reduced-dimension parametric control implemented with a realistic RIS to achieve performance close to that obtained in the idealized cases. The results demonstrate the ability of the reduced-dimension parametric control implemented with a realistic RIS to achieve performance close to that obtained in the idealized cases.

In particular, to emphasize the beam-steering capability of the wave-controlled RIS, we assume narrowband line-of-sight (LoS) channels with a single-antenna transmitter (Tx), K single-antenna receivers (Rx), and an RIS with M elements. Also, to focus on the behavior of the RIS, we assume there is no direct path between the Tx and Rx. We further assume far-field channels for the Tx-RIS and RIS-Rx links. In this case, the signal y_k at the k-th Rx will be given by the following signal expression assuming a transmitted signal s

$$y_k = \boldsymbol{h}_k^T \boldsymbol{\Phi} \boldsymbol{g} s + n_k , \qquad (1)$$

where n_k represents noise, h_k and g are respectively the $M \times 1$ channels from the RIS to the k-th Rx and the Tx to the RIS. The RIS response is defined by a diagonal matrix whose elements contain the reflection coefficients at the RIS elements:

$$\boldsymbol{\Phi} = \mathrm{diag}[\phi(0), \phi(1), \dots, \phi(M-1)]. \qquad (2)$$

As described in the next section, in a varactor-based implementation, the value of the m-th reflection coefficient $\phi(m)$ is determined by a biasing voltage applied to the m-th RIS element. Due to the passive nature of each element, the reflection coefficients satisfy $|\phi(m)| \leq 1$ for all $m = 0, 1, \dots, M - 1$. In the following, we will let $\boldsymbol{\phi} = [\phi(0), \phi(1), \dots, \phi(M-1)]^T$ denote the vector comprising the RIS reflection coefficients. The achievable values for the reflection coefficients as a function of frequency and varactor bias voltage are determined by considering mutual coupling under the local periodicity condition, as explained in [11] and also studied in [12], [13].

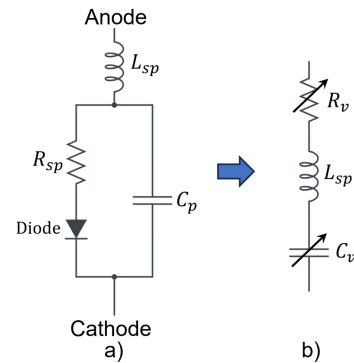## III. VARACTOR-BASED RIS REFLECTION MODEL
The general name for a reflective surface possessing subwavelength-size elements and intelligence to change its reflection properties is *metasurface* [8]. To demonstrate the metasurface's capability of programmable reflection phase shifts allowing for the control and redirection of incident
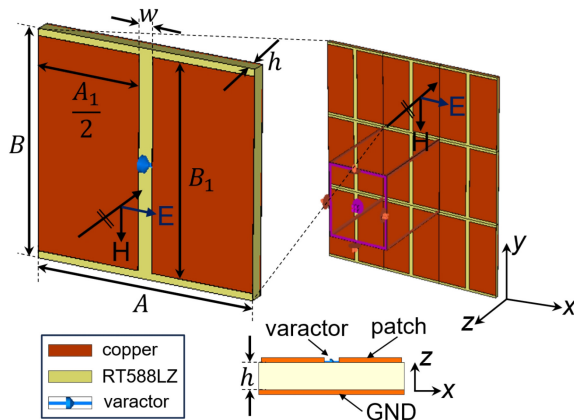
FIGURE 2. RIS formed by a periodic arrangement of square metallic conductors on a grounded dielectric substrate. The polarization of the incident electric field is along x. Varactor diodes are between patches, used as tunable capacitors when reverse biased.

FIGURE 3. Circuit model of the varactor. (a) SPICE model provided by the vendor. (b) Simplified equivalent RLC series (R_v (V), L_{sp}, C_v (V)) circuit model. The values of C_v and R_v vary with the applied bias voltage.

TABLE 1. Values of the equivalent capacitance and resistance of the varactor model in Fig. 3 (b) for different values of the varactor biasing voltage.

V (V)	C_v (pF)	R_v (Ω)
-15	0.460	0.005
-14	0.465	0.007
-13	0.471	0.011
-12	0.478	0.016
-11	0.488	0.024
-10	0.501	0.037
-9	0.519	0.058
-8	0.544	0.091
-7	0.578	0.142
-6	0.626	0.221
-5	0.697	0.340
-4	0.802	0.509

FIGURE 4. Equivalent capacitance and resistance of the varactor model in Fig. 3 (b) as a function of the varactor biasing voltage. Knowledge of these two functions of V leads to the analytic expression of the reflection coefficient $\phi_m(V)$ via (6), accounting for losses and RIS electromagnetic couplings.

plane waves, we consider an RIS made up of M elements along x with unit cells as shown in Fig. 2. Our nominal implementation of the RIS involves the use of square-shaped metal patches positioned on a grounded dielectric substrate. Varactors are placed at the center of each unit cell, connecting adjacent patches that are separated by gaps w. This design is a modified version of the dogbone-shaped metasurface discussed in [11], [14], where the magnetic resonance effect enables the tunability of the reflection coefficient phase. The geometry of the design is shown in Fig. 2 and uses the substrate Rogers RT5880LZ as a dielectric spacer, with relative permittivity $\epsilon_r = 2$ and loss tan $\delta = 0.0021$, and dimensions in mm given by $A = B = 19$, $A_1 = B_1 = 17.8$, $h = 1.27$, and $w = 1.2$.
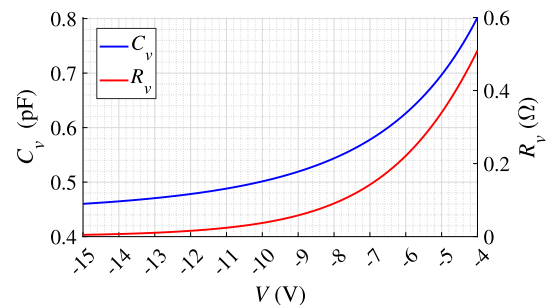
To achieve reconfigurable behavior for each unit cell, we employ the SMV1231-040LF varactor, provided by Skyworks Solutions, Inc. This specific varactor is chosen due to its desirable characteristics, including a low series inductance $L_{sp} = 0.45$ nH and resistance below 0.6 Ω, which are important for the intended design. The nonlinear varactor model obtained from the datasheet is shown in Fig. 3(a) and the small-signal model used in our equivalent RLC circuit model for the RIS is shown in Fig. 3(b), where, given varactor biasing voltage V, values for $R_v(V)$ and $C_v(V)$ are obtained from a parametric sweep simulation using Advanced Design System (ADS) software. In particular, the small-signal varactor impedance, Z_v, is computed from the S-parameter matrix of the model in Fig. 3(a) for different reverse-bias voltages and the results are fit to match the impedance of the series RLC circuit. In the simplified varactor model, the series inductance L_{sp} is the package inductance and it is static, and the two additional elements are defined as $R_v(V) = \mathrm{Re}(Z_v)$ and $C_v(V) = 1/(\omega^2 L_{sp} - \omega \,\mathrm{Im}(Z_v))$. The varactor capacitance tuning range is limited to $0.46 - 0.8$ pF, and the varactor resistance tuning range is limited to $0 - 0.6$ Ω. These parameters are detailed in Table 1 and illustrated in Fig. 4, where they are plotted as a function of the varactor biasing voltage.

A realistic RIS model is used to evaluate the reflection coefficient, as in [11], along the lines of [12]. The equivalent circuit model for plane wave reflection is shown in Fig. 5, where the parameters R_d, C_d, and L_d are the resistance, capacitance, and inductance associated with the square-shaped unit cell element, and the inductance L_s is an equivalent element that accounts for the grounded substrate, leading to the so called "magnetic resonance" as explored in [14] and also previously investigated in [15], [16]. The varactor is represented by the equivalent series RLC circuit model shown in Fig. 3(b).

The RIS equivalent impedance, Z_{eq}, seen by a plane wave without considering the varactor is given by

$$Z_{eq} = \left(R_d + j\omega L_d + \frac{1}{j\omega C_d}\right) || j\omega L_s. \tag{3}$$

This expression is rewritten as a function of the magnetic resonance, ω_m and electric resonance, ω_e, as

$$Z_{eq} = \frac{j\omega L_s\left(1 + j\omega R_d C_d - \left(\frac{\omega}{\omega_e}\right)^2\right)}{\left(1 + j\omega R_d C_d - \left(\frac{\omega}{\omega_m}\right)^2\right)}, \tag{4}$$

where $\omega_e^2 = 1/(C_d(L_d + L_s))$ and $\omega_m^2 = 1/(C_d L_d)$. We note that close to (but not at) ω_m the reflection phase is 0 degrees, and at ω_e, the reflection phase is almost 180 degrees, both studied in [14]. To acquire accurate numerical values for the elements L_d, C_d, and R_d, a single full-wave simulation without including the varactor is performed. The simulation models the RIS for plane wave orthogonal incidence by using a single cell with periodic boundary conditions, hence accounting for mutual couplings. It also accounts for dielectric and copper losses. The Z-parameters are evaluated from the S-parameters to obtain the values of ω_e and ω_m. The inductance $L_s = \mu_0 h = 1.6$ nH is analytically determined by modeling the substrate as a short-circuited transmission line section with a length of h and approximating the expression of the impedance as $Z_s = j\omega\tan(\mu_0 h) \approx j\omega\mu_0 h$. The other values are obtained as $L_d = L_s/((\omega_e/\omega_m)^2 - 1) = 0.39$ nH, $C_d = 1/(L_d\omega_e^2) = 0.53$ pF, and $R_d = L_s/(C_d(1 + L_d/L_s)\text{Re}(Z_{eq}(\omega_m))) = 0.08$ Ω.

The varactor included in the analytical model is in parallel to the capacitor C_d that models the capacitance created by the gap across which the varactor is connected. Note that the inductance $L_v = L_{sp} + L_p = 2.34$ nH replaces the inductance L_{sp}. The term L_p represents the parasitic inductance introduced by the varactor when connected across the gap in the full-wave simulations, which will be presented later. Therefore, the total equivalent RIS impedance, Z_{RIS}, is given by

$$Z_{RIS} = \left(R_d + j\omega L_d + \left(R_v + j\omega L_v + \frac{1}{j\omega C_v}\right) || \frac{1}{j\omega C_d}\right) || j\omega L_s, \tag{5}$$

and the reflection coefficient, ϕ, is evaluated as

$$\phi = \frac{Z_{RIS} - Z_0}{Z_{RIS} + Z_0}, \tag{6}$$

where Z_0 is the free-space impedance.

In order to assess the performance of the proposed analytical model, the commercial CST Studio Suite[2] software package is used to obtain the reflection coefficient from full-wave simulations, including the effect of the varactor as a lumped load. The magnitude and phase of the reflection coefficient for various varactor reverse bias voltages are plotted in Fig. 6, demonstrating the capability of the circuit model to estimate the reflection coefficients for various

---

[2]CST Studio Suite is a portfolio of electromagnetic field solvers.
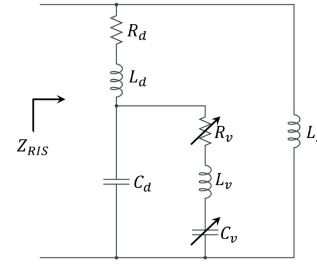

FIGURE 5. Equivalent analytical circuit model of the RIS. Z_{RIS} is seen from the left.
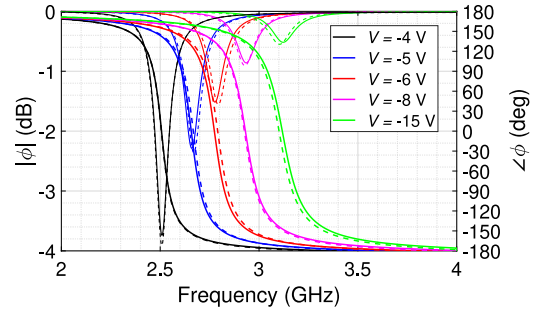

FIGURE 6. Magnitude and phase of the RIS reflection coefficient varying varactor's biasing voltage, calculated using the equivalent circuital analytical model (solid lines), and compared with the results of the full-wave simulation (dashed lines). The analytical model accounts for metallic and substrate losses as well as losses in the varactors. It also accounts for electromagnetic couplings among the RIS elements, calculated based on the local periodicity approximation. Model and full-wave simulations are in good agreement.
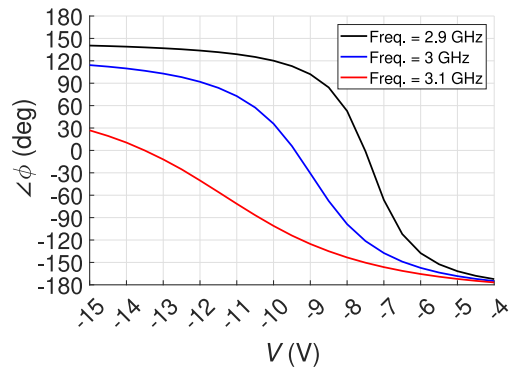

FIGURE 7. Phase of the RIS reflection coefficient as a function of the biasing voltage applied to the varactor for three different frequencies.

frequencies and varactor voltages. The results demonstrate that a phase dynamic range (defined as the set of phase values that can be obtained at a given frequency) of around 290° is activated in the band between 2.6 GHz–3 GHz. The phase of the RIS reflection coefficient as a function of the biasing voltage applied to the varactor for three different frequencies is shown in Fig. 7, where a tradeoff between the phase dynamic range and the biasing voltage range can be observed.

IV. WAVE-CONTROLLED RIS (FULL-DOMAIN CONTROL BASIS)

We show that individual control on the biasing voltage is achieved using a superposition of full-domain functions,

$w(x, t) = \sum_n w_n(x, t)$, over the whole RIS length as shown in Fig. 1. In particular, we use a set of N standing waves over the whole length of the RIS, written as

$$w(x, t) = W_0 + \sum_{n=1}^{N} W_n \sin\left(\frac{n\pi(x + L_{left})}{L_{tot}}\right) \sin(n\omega_b t), \quad (7)$$

where N represents the number of full-domain expansion modes in the bias voltage decomposition and W_n is the amplitude of the n-th mode, $n = 0, 1, \ldots, N$. The vector of coefficients $W = [W_0, W_1, \ldots, W_N]^T$ is used to parameterize the biasing voltage. We consider $L_{tot} = L + L_{left} + L_{right}$ because the two extra segments on the left and right of the biasing transmission line (TL) are useful to better control the voltage values on the RIS over the length L. Note that (7) corresponds to a *truncated* Fourier series in space, with N, rather than an infinite number of sinusoids. What is shown in (7) is a signal that will be generated in the biasing TL for control of the RIS that, when sampled, will yield the needed bias voltage at each RIS element. For this reason, the value of N is desired to be as small as possible to limit the variation in $w(x, t)$ with x, and also to reduce the control signaling overhead. The biasing voltage is sampled along the biasing TL and applied as inputs to the RIS elements' varactors at positions $x_m = md_x$, $m = 0, 1, \ldots, M - 1$, where d_x is the distance between the centers of each pair of adjacent RIS elements.

In the development of the biasing TL, it is convenient to use low frequencies for the standing waves, much smaller than the RIS operation frequency that is either in the cm-wave (i.e., microwave) or in the mm-wave range. This is achieved by considering a slowness factor n_{slow} of the waves in the biasing TL that is dependent on the materials used and the actual geometry of the biasing TL. Therefore, in the biasing TL, the phase velocity of the waves along the x direction is equal to $v_{ph} = c/n_{slow}$, where c is the speed of light. The fundamental standing wave depicted by $w_1(x, t)$ in Fig. 1 is such that $k_b L_{tot} = \pi$, where $k_b = \omega_b/v_{ph}$ is the wavenumber, ω_b is the angular frequency, and L_{tot} is the total length of the biasing TL in the x direction. Therefore, the fundamental standing wave oscillates at $f_b = \omega_b/(2\pi)$ where $\omega_b = \pi v_{ph}/L_{tot}$ [17]. A simple choice of parameters can produce a value for f_b in the low MHz range. Higher order standing waves $w_n(x, t)$, $n = 2, 3, \ldots, N$, oscillate at frequencies nf_b, with wavenumbers $k_{b,n} = nk_b$, $n = 1, 2, \ldots, N$. In this model, we assume that $0 \leq x_m \leq L$, $m = 0, 1, \ldots, M - 1$.[3] For notational convenience, the standing

[3] In reality, the TLs underneath the RIS surface have different lengths between the RIS elements than on the RIS surface. In our experimental implementation, we use a serpentine structure for TL. This is done to reduce spatial sensitivity in realizing the TLs. Let us say the length of the TL between two adjacent RIS elements is d_x. Then $L = (M - 1)d_x$, $L_{left} = M_l d_x$, $L_{right} = M_r d_x$ where M_l and M_r are nonnegative numbers, and $L_{tot} = L + L_{left} + L_{right}$.
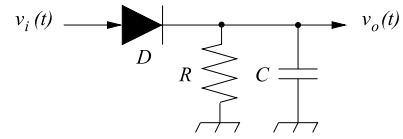
FIGURE 8. Rectifier circuit used to rectify the alternating current voltage on the biasing TL. The input voltage $v_i(t)$ is the standing waves at location m; the output voltage $v_o(t)$ is the rectified voltage to bias the varactor at location m. The circuit follows the envelope or the peak of $v_i(t)$ via the diode D, the resistor R, and the capacitor C. The time constant RC should be chosen sufficiently large to keep the capacitor discharge to manageable levels so that $v_o(t)$ does not show a significant drop between the consecutive peaks of $v_i(t)$. (This circuit is not present when the sample-and-hold technique is used, as described later on.)

waves in (7) are rewritten directly in terms of m as

$$w(md_x, t) = W_0 + \sum_{n=1}^{N} W_n \sin\left(\frac{n\pi(m + M_l)}{M - 1 + M_l + M_r}\right) \sin(n\omega_b t), \quad (8)$$

where $M_l = L_{left}/d_x$ and $M_r = L_{right}/d_x$.

A. ENVELOPE DETECTOR CIRCUIT

A potential way to detect the voltage level needed for biasing the varactors is by using the rectifier circuit shown in Fig. 8, one per RIS element. This is a conventional circuit element employed in communications electronics, most commonly to demodulate an amplitude-modulated continuous-time signal. Its operating principles are simple, see, e.g., [18]. Typically, the time constant RC is chosen such that

$$\frac{1}{f_N} \ll RC \ll \frac{1}{f_{reconfig}} \quad (9)$$

where f_N is the highest frequency of the sinusoidal signal in the biasing TL (i.e., related to the highest n-harmonic). The value for $f_{reconfig}$ is the frequency at which the RIS needs to be reconfigured. This condition ensures the circuit is able to follow the envelope of the highest-frequency sinusoid in the biasing TL. We employ the envelope detector to perform a peak detection of the standing wave signal which oscillates with time t.

The standing waves on the biasing transmission line of the RIS oscillate in time with frequencies nf_b as $\sin(n\omega_b t)$, hence the highest frequency is $f_N = Nf_b$.

To only sample the peak of the standing wave at each element m over time, the rectifier outputs are simply described here by taking the peak (maximum) values of the alternating time domain signal, as

$$w(m) = \max_t \left(W_0 + \sum_{n=1}^{N} W_n \sin\left(\frac{n\pi(m + M_l)}{M - 1 + M_l + M_r}\right) \sin(n\omega_b t)\right), \quad (10)$$

where $w(m)$ represents the DC voltage bias supplied to each varactor index using the standing waves. We observe that the envelope of the time-varying part inside the parenthesis in (10) is symmetric in its positive and negative ranges. Since varactors are polarized inversely, we have decided to work with the negative part of the envelope and thus in the sequel, we will replace max in (10) with min. In addition, since the
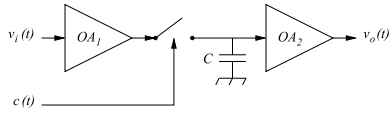
FIGURE 9. Sample-and-hold circuit to bias the varactors. The input voltage $v_i(t)$ is the biasing standing waves at location m; the output voltage $v_o(t)$ is used to bias the varactor at location m, and the control signal is $c(t)$. OA_1 and OA_2 are operational amplifiers, and C is the capacitance that holds the sampled voltage. (This circuit is not present when we use the rectifiers.)

DC level of the standing wave is independent of time, the expression is simplified to

$$w(m) = W_0 + \min_t \left(\sum_{n=1}^{N} W_n \sin\left(\frac{n\pi(m+M_l)}{M-1+M_l+M_r} \right) \sin(n\omega_b t) \right). \quad (11)$$

Due to the min function, using rectifiers implies a nonlinear relationship between the standing wave coefficients W_n and the spatial voltage levels $w(m)$.

B. SAMPLE-AND-HOLD CIRCUIT

Another potential way to detect the voltage level needed for biasing the varactors is by using sample-and-hold (SH) circuits shown in Fig. 9. In this approach, every RIS element employs an SH circuit to sample the standing wave along the transmission line and hold it for a given duration to configure the corresponding RIS element. The SH is a standard circuit element used in many applications, for example, in analog-to-digital converters [19]. A conceptual diagram is provided in Fig. 9 where the input voltage $v_i(t) \equiv w(md_x, t)$ is sampled at the output of the operational amplifier OA_1 under the control of the signal $c(t)$. This signal is held in the capacitor C such that it can be read out at the output of the operational amplifier OA_2 as the bias voltage for the varactor diode controlling the phase of the RIS element. These circuits are used in analog-to-digital converters to eliminate variations in an input signal because such variations can corrupt the conversion. As shown in Fig. 9, an SH circuit has a switching device such as a transistor which loads the capacitor C with the sampled voltage. This happens during the *sample* stage of the circuit when the buffer amplifier OA_1 charges or discharges the capacitor and makes the voltage across C equal to the sampled input voltage. In the next stage, the *hold* stage, the switch disconnects the capacitor from OA_1, which can be read out by OA_2. It is possible that the capacitor can discharge through the load it sees at the input of OA_2 and its own leakage, but this can be made to take a long time.

1) DISTRIBUTION OF THE SAMPLING SIGNAL

Only a single control signal is required for the SH circuits at each element, since they can be sampled at or near the same time. A coaxial cable connection can be used to eliminate interference between the control and standing wave signals. The sampling signal requires less bandwidth than the standing wave. This simple configuration assumes all RIS elements are provided with the same sample timing. Even if different sampling times are used at different RIS elements, it is possible to orthogonalize the signal. The coaxial cable will prevent interference as long as the cut-off frequency is not approached.

An alternative for distribution of the sampling signal is wireless transmission. In such a system, the wireless module would be connected to the control inputs of the analog switches responsible for the operation.

2) DISTRIBUTION OF POWER

The power can be distributed by a single-wire DC distribution circuit. It is possible to carry out this power distribution such that the possibility of RF interference can be avoided. In fact, the same coaxial cable for distribution of the sampling signal can also carry the DC power. It is possible that some SH circuits would require more than one voltage level. In that case, use of more than one cable is possible, or multiple DC voltages can be derived from a single voltage source. We note that the SH circuits are in general not power hungry, and therefore, distribution of power will not require a substantial effort.

As an alternative, power can be locally generated at each RIS element by means of energy harvesting. For example, energy can be harvested from light and stored at night. Or energy can be harvested from received RF energy. Yet another alternative is to use batteries with replacement; for example, one can alternate between two batteries for hitless operation. Reference [20] discusses the use of RFID tags to power the entire RIS.

3) DESIGN OF SAMPLE-AND-HOLD CIRCUITS

A number of criteria need to be judiciously applied to the design of an SH circuit. Examples are switching speed, settling times, aperture time, jitter and noise, input range, power consumption, etc.

V. OPTIMIZATION ALGORITHMS

In the communication theory literature, algorithm design for RIS optimization has almost exclusively employed simplistic models in which one has the ability to directly and independently control the reflection coefficient $\phi(m)$ of each RIS element. In reality, the actual control signal at the m-th unit cell is (for example) a biasing voltage $V(m)$ on a varactor diode, and as shown in the realistic unit cell model presented earlier, arbitrarily tuning the phase of $\phi(m)$ is not possible. Furthermore, in the approach considered here, $V(m)$ is obtained by sampling a set of standing waves $w(md_x, t)$ using a device that is neither linear nor time variant. As a result, compared with conventional RIS optimization methods, it is significantly more challenging to design the weights W_n to produce a standing wave $w(md_x, t)$ that when sampled yields a voltage $V(m)$ that in turn generates the desired RIS response $\phi(m)$. Achieving this goal requires approaches entirely different from those proposed to date in the literature which only consider optimization of $\boldsymbol{\phi}$ directly. In this section we present the results of several algorithms

for solving this problem that differ based on the desired performance metric and the type of sampling circuit used to extract the varactor biasing. We focus on scenarios where the RIS is designed to form beams or nulls in certain directions in response to a line-of-sight signal from a transmitter.

A. MATHEMATICAL FORMULATION OF THE OPTIMIZATION PROBLEM

For the purpose of describing the optimization of the proposed RIS architecture, we assume that the direct propagation path between the transmitter and each UE is either already known or assumed to be nonexistent, and we only consider the path reflected by the RIS. Let the narrowband flat fading channel between the single-antenna transmitter and RIS element m be described by $g(m)$ and that between RIS element m and the k-th single-antenna UE be $h_k(m)$. We assume perfect knowledge of $h_k(m)$ and $g(m)$ for all K receivers and all M RIS elements. Then, the expression for the signal received by UE k is

$$y_k = \left[\sum_{m=0}^{M-1} h_k(m)\phi(m)g(m) \right] s_k + n_k , \qquad (12)$$

where $\phi(m)$ is the reflection coefficient at the m-th RIS element, s_k is the transmitted signal, and n_k is additive white Gaussian noise (AWGN), i.e., $n_k \sim \mathcal{CN}(0, \sigma_s^2)$. Writing this in matrix form, we have

$$y_k = \boldsymbol{h}_k^T \boldsymbol{\Phi} \boldsymbol{g} s_k + n_k \qquad (13)$$

where $\boldsymbol{h}_k = [h_k(0), h_k(1), \ldots, h_k(M-1)]^T$ and $\boldsymbol{g} = [g(0), g(1), \ldots, g(M-1)]^T$ are respectively the $M \times 1$ channels from the RIS to UE k and the BS to the RIS, and the RIS response is described by the diagonal matrix $\boldsymbol{\Phi} = \text{diag}[\phi(0), \phi(1), \ldots, \phi(M-1)]$. Each $h_k(m) = \alpha_k(m)e^{-j\theta_k(m)}$ and $g(m) = \beta(m)e^{-j\psi(m)}$. Since the RIS elements are passive (their reflection coefficients are only determined from the capacitance supplied by the varactors), $|\phi(m)| \leq 1$ for all $m = 0, 1, \ldots, M-1$.

The signal-to-noise ratio (SNR) at UE k is the ratio of the received signal power divided by the noise power σ_s^2

$$\text{SNR}_k = \frac{|E[y_k]|^2}{\sigma_s^2} = \frac{|E[\boldsymbol{h}_k^T \boldsymbol{\Phi} \boldsymbol{g} x]|^2}{\sigma_s^2} = \frac{\rho_s |\boldsymbol{h}_k^T \boldsymbol{\Phi} \boldsymbol{g}|^2}{\sigma_s^2} \quad (14)$$

where ρ_s is the average power for each transmitted symbol. To evaluate the ability of the proposed wave-controlled RIS to configure the wireless channels to the UEs, we will consider optimizing the RIS configuration $\boldsymbol{\Phi}$ for the two objective functions described below.

1) Maximize the SNR for a given UE:

$$\max_{\boldsymbol{\eta}} \text{SNR} = \max_{\boldsymbol{\eta}} \rho_s |\boldsymbol{h}_k^T \boldsymbol{\Phi} \boldsymbol{g}|^2 , \qquad (15)$$

where $\boldsymbol{\eta}$ is a parameter vector that represents the variables that control the RIS configuration $\boldsymbol{\Phi}$. These variables can be the reflection coefficients themselves ($\boldsymbol{\eta} = \boldsymbol{\phi} = [\phi(0), \phi(1), \ldots, \phi(M-1)]^T$),

the biasing voltages at the varactors ($\boldsymbol{\eta} = \boldsymbol{V} = [V(0), V(1), \ldots, V(M-1)]^T$), or amplitudes of the modes that define the biasing waveforms ($\boldsymbol{\eta} = \boldsymbol{W} = [W_0, W_1, \ldots, W_N]^T$).

2) Maximize the worst-case signal-to-leakage-plus-noise ratio (SLNR) for a certain combination of desired and undesired receivers:

$$\max_{\boldsymbol{\eta}} \text{SLNR} = \max_{\boldsymbol{\eta}} \frac{\min_{i \in \{1,2,\ldots,K\}} \rho_s |\boldsymbol{h}_{d,i}^T \boldsymbol{\Phi} \boldsymbol{g}|^2}{\max_{j \in \{1,2,\ldots,L\}} \rho_s |\boldsymbol{h}_{e,j}^T \boldsymbol{\Phi} \boldsymbol{g}|^2 + \sigma_s^2}. \qquad (16)$$

where $\boldsymbol{h}_{d,i}$ are the channels between each RIS element and each desired Rx, and $\boldsymbol{h}_{e,j}$ are the channels corresponding to undesired or "eavesdropping" receivers. The worst-case SLNR is calculated using the minimum power reflected towards any of the K desired receivers, divided by the summation of the noise power and the maximum power reflected towards any of the L undesired receivers.

In order for the analytical model to match the physical RIS model created from our full-wave simulations, the following assumptions are made for the numerical examples [17]

- The RIS is arranged as a uniform linear array with elements separated by Δ, which is in terms of wavelengths, and therefore a unitless quantity.
- The BS is located in the far field in the direction of the broadside of the RIS, such that there is normal incidence between the BS and each RIS element, and hence

$$\boldsymbol{g} = [1, 1, \ldots, 1]^T.$$

- The UE is located at an azimuth angle of θ^* from the RIS and hence

$$\boldsymbol{h}(\theta^*) = \left[1, e^{-j\kappa(\theta^*)}, e^{-j2\kappa(\theta^*)}, \ldots, e^{-j(M-1)\kappa(\theta^*)} \right]^T$$

where $\kappa(\theta) = 2\pi\Delta\sin(\theta)$. We will assume a specific case with a carrier frequency of $f_c = 3$ GHz and a spacing of 19 mm between RIS elements. At $f_c = 3$ GHz, this corresponds to a Δ of about $1/5 = 0.2$. Vector $\boldsymbol{h}(\theta^*)$ assumes line-of-sight channels to the users, though this is not strictly necessary.

B. OPTIMIZATION PROBLEM 1: MAXIMIZING SNR AT A SINGLE UE DIRECTION
1) IDEAL PHASE

In this case, assume that each individual reflection coefficient $\phi(m)$ can be modified to any value such that $|\phi(m)| = 1$, so there is full control over the phase shift of the reflected wave. The task is to find $\boldsymbol{\Phi}$ such that the expression $P = \rho_s |\boldsymbol{h}^T \boldsymbol{\Phi} \boldsymbol{g}|^2$ is maximized.

For this analysis, the average transmission power ρ_s can be ignored since the RIS has no impact on ρ_s and does not provide any amplification or attenuation due to its reflective nature. For the flat fading model $h(m) = \alpha(m)e^{-j\theta(m)}$ and

$g(m) = \beta(m)e^{-j\psi(m)}$, the power is maximized when $\phi(m) = e^{j(\theta(m)+\psi(m))}$, since this produces a coherent sum:

$$P = \rho_s \left| \sum_{m=0}^{M-1} h(m)\phi(m)g(m) \right|^2$$

$$= \rho_s \left| \sum_{m=0}^{M-1} \alpha(m)e^{-j\theta(m)} e^{j(\theta(m)+\psi(m))} \beta(m)e^{-j\psi(m)} \right|^2$$

$$= \rho_s \left| \sum_{m=0}^{M-1} \alpha(m)\beta(m) \right|^2. \tag{17}$$

2) ARBITRARY VOLTAGE BIAS

Since the varactor diodes have voltage limits, some of the phase values may not be achievable, as seen in Fig. 6–Fig. 7. Taking this constraint into account, the objective should be to set the bias voltage such that the resulting phase is as close as possible to the ideal phase of the previous case. We see from Fig. 7 that for frequencies in the range 2.9–3.1 GHz, the mapping from the varactor voltage to the reflection coefficient phase is a one-to-one function. Let $\varphi(V(m))$ be the one-to-one mapping that converts the varactor voltage $V(m)$ into RIS reflection coefficient phase $\angle\phi(m)$ for RIS element m. Then, the phases are bounded between $\angle\phi_{min} = \varphi(V_{max})$ and $\angle\phi_{max} = \varphi(V_{min})$. Therefore, the phases obtained by the biasing voltages become

$$\angle\phi_{arb} = \begin{cases} \angle\phi_{min} & \text{if } \angle\phi_{ideal} < \angle\phi_{min}, \\ \angle\phi_{ideal} & \text{if } \angle\phi_{min} \le \angle\phi_{ideal} \le \angle\phi_{max}, \\ \angle\phi_{max} & \text{if } \angle\phi_{ideal} > \angle\phi_{max}. \end{cases} \tag{18}$$

The "arbitrary voltages" that reproduce these phase shifts are

$$V = \varphi^{-1}(\angle\phi_{arb}). \tag{19}$$

For the simulations to be presented later, the inverse mapping $\varphi^{-1}(\cdot)$ is obtained by linearly interpolating the phase values obtained for a set of discrete biasing voltages spaced with steps of 5mV. For the model described in Section III, the biasing voltage range is $[-15V, -4V]$. We assume that the varactor diodes are inversely biased. Thus, the voltage values can be interchangeably represented by positive numbers for the same range of absolute values.

C. SOLUTION FOR OPTIMIZATION PROBLEM 1: ENVELOPE DETECTOR

Recall that in the envelope detector model, only the peak of the standing wave voltage $w(x_m, t)$ at each varactor is converted into a sampled DC voltage. For negative biasing voltages, the most negative voltage is considered to be the peak (minimum). Therefore, the voltage at each varactor is modeled as in (11) which tracks the negative signs.

The problem of finding the weights to produce a desired peak voltage is a difficult nonlinear optimization problem that cannot be solved analytically. To cover the full range of the varactor biasing voltages, $\min_t(\cdot)$ will always produce
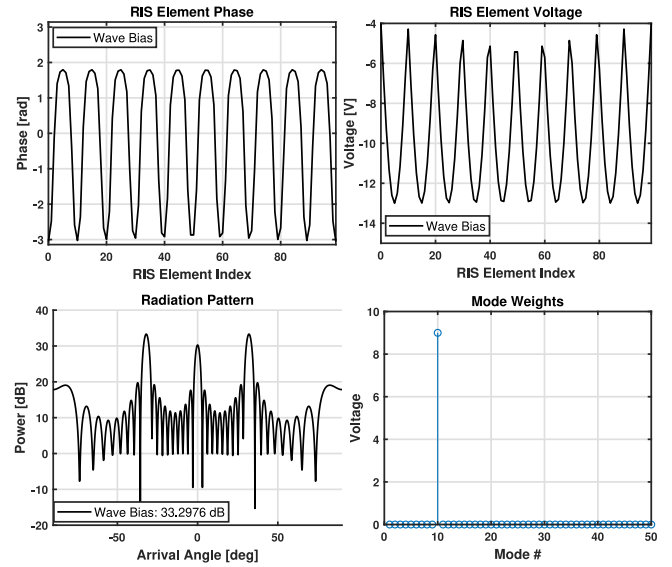
FIGURE 10. Envelope detector model with only one mode activated. Bottom right: $W_{10} = 9V$, while the other mode amplitudes are zero. Top right: DC voltages across all 100 varactors, after rectification. Top left: Reflection phases created at each element. Bottom left: Resulting radiation pattern for a wide range of arrival angles.

a negative voltage, so W_0 should be set to the maximum voltage level (in this case, $-4V$). Of the multiple approaches that we have explored to maximize the power towards a single receiver, a combination of the two algorithms described below has proven to be fruitful.

1) ALGORITHM 1 - WEIGHT RANKING

The motivation for this approach began with the observation that increasing only a single mode amplitude can greatly enhance power reflected towards a given direction, though changing one mode would not achieve the global solution since all the elements must be utilized accurately, requiring more dimensions for the optimization by wave biasing. It was noted that there was a correlation between the frequency of the mode whose amplitude was increased and the direction towards which the RIS reflected the signal, as seen in Fig. 10. Just by increasing the amplitude for mode #10 (W_{10}) to 9V, without any contribution from the other modes, a gain of around 33.3 dB at both $32°$ and $-32°$ was observed. Based on this, we developed the *Weight Ranking* algorithm, which ranks the weights by their importance to maximize power reflected towards a single desired receiver direction θ^*. The algorithm is implemented as specified in Algorithm 1 with complexity $\mathcal{O}(kN + N\log N)$, where k is the number of times each mode amplitude is incremented or decremented until the power has been maximized. The value of k depends on the choice of the step size, which is 0.001 in our implementation.

2) ALGORITHM 2 - BRUTE FORCE OPTIMIZATION

This algorithm takes the indices that correspond to the most influential amplitudes as determined in Algorithm 1. It uses a hill-climber approach to converge towards optimal

Algorithm 1 Weight Ranking

1: $W \leftarrow [0, 0, \ldots, 0]^T$ (array containing N amplitudes)
2: $W_0 \leftarrow -4\text{V}$
3: $P_{arr} \leftarrow [0, 0, \ldots, 0]$ (array containing N entries of power measurements at the desired receiver angle)
4: **for** each $n \in \{1, \ldots, N\}$ **do**
5:     Find the value for the weight $W(n)$ that maximizes the power at θ^* by either increasing or decreasing the amplitude by 0.001 and calculating the voltage curve and power gain.
6:     Record the maximal power in $P_{arr}(n)$
7:     Reset $W = [0, 0, \ldots, 0]^T$
8: **end for**
9: Sort P_{arr} in descending order and extract the indices n that correspond to power values from highest to lowest that can be mapped later to corresponding amplitudes $W(n)$.

Algorithm 2 Brute Force

1: $W \leftarrow [0, 0, \ldots, 0]^T$
2: $W_0 \leftarrow -4$
3: calculate $w(m)$ using (11), $m = 0, 1, \ldots, M - 1$
4: $P_{old} \leftarrow$ initial power reflected towards θ^* using $w(m)$
5: $\mu \leftarrow 1.0$ (initial step size)
6: "negate" $\leftarrow 0$ (Boolean value that determines if the current step is positive or negative)
7: **repeat**
8:     **for** each $W(n)$, starting from the highest power index to the lowest power index obtained from Algorithm 1 **do**
9:         $W_{new}(n) \leftarrow W(n) + \mu$
10:         Calculate $w_{new}(m)$
11:         **if** $w_{new}(m)$ has elements outside the interval $[-15, -4]$ **then**
12:             **if** "negate" $== 0$ **then**
13:                 $\mu \leftarrow -\mu$
14:                 "negate" $\leftarrow 1$
15:                 Go back to step 9
16:             **else**
17:                 $\mu \leftarrow -\mu$
18:                 "negate" $\leftarrow 0$
19:                 Go back to step 8 for the next $W(n)$
20:             **end if**
21:         **end if**
22:         Calculate P_{new} using updated $w_{new}(m)$
23:         **if** $P_{new} > P_{old}$ **then**
24:             $W \leftarrow W_{new}$
25:             $P_{old} \leftarrow P_{new}$
26:             $w(m) \leftarrow w_{new}(m)$ for all m
27:         **else**
28:             Perform the steps starting at line 12
29:         **end if**
30:     **end for**
31:     $\mu \leftarrow \frac{\mu}{2}$
32: **until** $\mu \geq 0.001$

amplitude weights by increasing or decreasing each weight according to the order that was previously obtained [21]. The weights are ordered before using the hill-climber approach since the order of the amplitudes matters when optimizing. First, there is the constraint that the voltage must stay within the range $[-15V, -4V]$ so the summation of the weights is also constrained. Second, increasing the weights in a different order may cause the waveform to change so that the contributions of the corresponding modes to the radiation pattern changes, due to the nonlinear relationship created by the $\min_t(\cdot)$ operation. The complexity of this algorithm is approximated by $\mathcal{O}(MN \log \frac{1}{\mu_f})$, where μ_f is the final value of the step size μ (in this case, 0.001), assuming μ starts at 1.

3) SIMULATION RESULTS

The Weight Ranking and Brute Force algorithms were implemented in MATLAB.[4] The RIS configuration and the optimization goal are as follows. A spacing of 19 mm between the RIS elements is employed, $f_c = 3$ GHz, and $f_b = \omega_b/(2\pi) = 12.9$ MHz. There are $M = 100$ RIS elements and $N = 50$ modes used to construct the voltage waveform. The array is extended by $2d_x$ at each of its ends, without placing varactors at these locations, simulating the waveform going through a longer path along the transmission line ($M_l = M_r = 2$). There is one desired receiver direction at $\theta^* = -30°$.

One advantage of the Weight Ranking and Brute Force algorithms is that they do not require any prior knowledge on the shape of the desired voltage waveform to find an optimal set of weights. Rather, they simply attempt to increase the SNR for a given desired direction. The results of this approach versus the ideal phase values and their
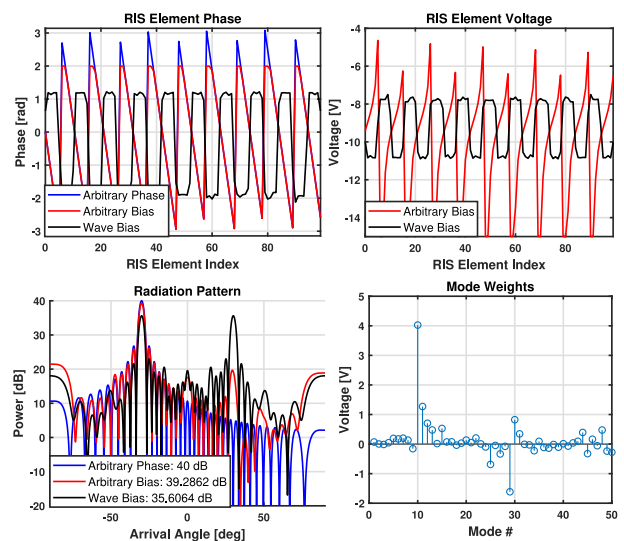
---

[4]MATLAB is a programming and numeric computing platform to analyze data, develop algorithms, and create models.
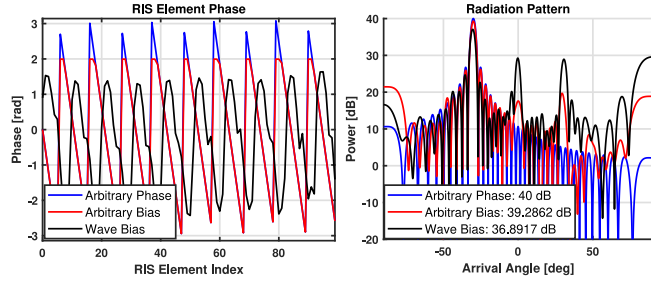

FIGURE 11. Maximizing SNR towards single receiver at −30° using Weight Ranking and Brute Force algorithms.

corresponding arbitrary voltage values have been compared in Fig. 11.

It can be seen in Fig. 11 that there is a 3.7 dB loss between the model that uses the arbitrary voltage values and

FIGURE 12. Maximizing SNR towards single receiver at $-30°$ using Weight Ranking and Brute Force algorithms, with $M_l = 2$ and $M_r = 102$.

the wave-controlled approximation. The only resemblance between the standing-wave model and the ideal models in the voltage and phase curves is that the spatial frequency of the standing waves matches; otherwise the standing-wave model appears more like a square wave than the ideal sawtooth-shaped waveform. In addition to the desired peak at $-30°$, there is a phantom peak at $30°$ due to the symmetry in the voltage waveforms, as the curves appear to be mirrored around the 50th RIS element. One way to eliminate this symmetry would be to double the length of the transmission line without adding more elements, but this would require doubling the length of the physical structure without increasing the SNR gain. When increasing the length by $2d_x$ on one side of the array and $102d_x$ on the other, the radiation pattern shown in Fig. 12 results, yielding a weaker peak at $30°$ that is approximately 8.4 dB lower than for the desired direction. However, the additional gain at $-30°$ compared to the previous case is only around 1.3 dB. Interestingly, the phase curve of the standing wave model more closely resembles that of the ideal model, with some differences in the spatial phase shifts and amplitudes of the standing waves, likely due to the use of an insufficient number of high frequency components to construct the waveform. A disadvantage of this algorithm is that not all of the modes are being fully employed; only a few of the modes have high-amplitude weights, while many others are near zero. This is an inherent weakness of the hill-climber algorithm as it tends to converge to a local minimum while not exploring different combinations of weights. Alternative algorithms such as Simulated Annealing may provide better performance.

D. SOLUTION FOR OPTIMIZATION PROBLEM 1: SAMPLE-AND-HOLD CIRCUIT

1) STANDING WAVE BIAS - USING SAMPLE-AND-HOLD MODEL

A sample-and-hold (SH) circuit at each RIS element can be used to sample the standing wave voltage in (8) at a specific time instant, and hold that voltage until the next sampling cycle. Assume that all RIS elements are sampled at the same arbitrary time t_0 such that $\sin(n\omega_b t_0) \neq 0$, $n = 1, 2, \ldots, N$. Then, the $\sin(n\omega_b t_0)$ terms in the modal expansion are no more than just weighting factors for each W_n, leading to

$$w(m) = w(md_x, t_0). \qquad (20)$$

To match the wave modes with the arbitrary voltage waveform defined in Section V-B2, a Least Squares (LS) algorithm is derived below. As before, the length of the transmission line was extended at either end of the RIS to eliminate the boundary conditions and improve the match between the original waveform and that generated by the limited modes. For ease of implementation, the waveform generated by the sinusoids is centered around the average voltage of the arbitrary voltage bias $V(m)$ that would ideally be supplied to each varactor index m,

$$W_0 = \frac{1}{M} \sum_{m=0}^{M-1} V(m). \qquad (21)$$

Then, the variable W_0 is removed from the LS optimization and the objective function becomes

$$\min_{W} J = \min_{W} \sum_{m=0}^{M-1} ||w(m) - V(m)||_2^2 \qquad (22)$$

where $W = [W_1, W_2, \ldots, W_N]^T$ is the column vector containing the mode amplitudes. The LS solution is

$$W = \left(\sum_{m=0}^{M-1} s_m s_m^T \right)^{-1} \left(\sum_{m=0}^{M-1} (V(m) - W_0) s_m \right) \qquad (23)$$

where

$$s_m = \left[\sin\left(\frac{\pi(m + M_l)}{M - 1 + M_l + M_r} \right) \sin(\omega_b t_0), \ldots, \right.$$
$$\left. \sin\left(\frac{N\pi(m + M_l)}{M - 1 + M_l + M_r} \right) \sin(N\omega_b t_0) \right]^T. \qquad (24)$$

Please refer to Appendix A for the derivation of the algorithm.

2) SAMPLE-AND-HOLD MODEL SIMULATION RESULTS

We simulate the LS algorithm for an RIS with $M = 100$ elements using $N = 50$ sinusoidal modes. The variable t_0 was chosen as $\frac{8}{\omega_b}$ which guarantees that $\sin(n\omega_b t_0) \neq 0$, $n = 1, 2, \ldots, 50$. As before, we assume a far-field wave with normal incidence and a desired receiver located at an azimuth angle of $-30°$ from the RIS. To eliminate edge effects, the transmission line is $2d_x$ longer on either side of the board ($M_l = M_r = 2$).

Fig. 13 plots the results for this case. Compared to the radiation pattern generated using the arbitrary voltage bias, the wave-controlled approach has 2.4 dB less beamforming gain in the desired direction. The radiation patterns generally look similar and the spurious peaks at $0°$ and $30°$ are much smaller than in the case of the envelope detector. The performance of the LS algorithm can be improved by taking into account the fact that certain biasing voltages are more important for differentiating the RIS phase response. As seen in Fig. 7, especially for carrier frequencies of 2.9 and 3 GHz, the sensitivity of the phase is much higher for certain voltage ranges. For example, for 3 GHz, biasing voltages between $-6V$ and $-9V$ produce very large changes in the
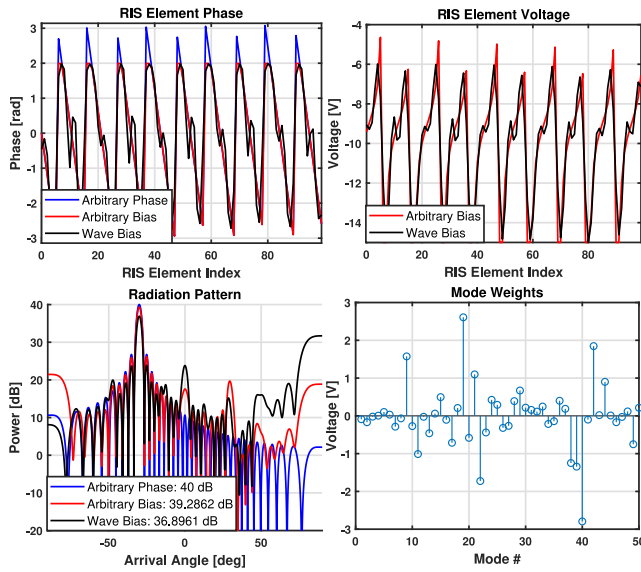
FIGURE 13. Maximizing SNR towards single receiver at −30° with LS approach.
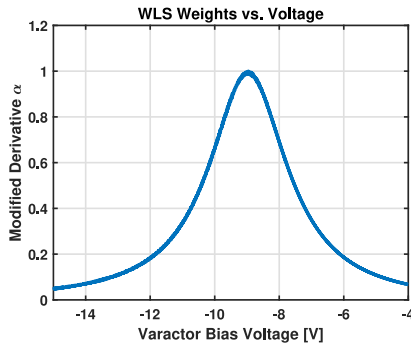

FIGURE 14. Modified phase versus voltage derivatives as weights for WLS.

phase, while voltages less than −9V result in much less variation. As explained in the next section, this sensitivity can be exploited by weighting the importance of the biasing voltages in the LS optimization.

3) WEIGHTED LS

Clearly, the sensitivity of the phase to changes in the biasing voltage is reflected by the slope of the biasing curves in Fig. 7, and thus a reasonable way to assign the weights is based on this slope. First, we discretize the voltage values between −15V and −4V in 1mV steps and calculate the derivative of the reflection phases with respect to DC voltage bias. Then, we normalize the results between 0 and 1 and add 0.001 to each normalized derivative to eliminate possible zero weights. The final weight, $\alpha(m)$, corresponding to each RIS element m, is defined as

$$\alpha(m) = \frac{\left|\frac{\varphi(V(m)) - \varphi(V(m)+0.001)}{0.001}\right|}{\max_{V \in \{-15, -14.999, \ldots, -4\}} \left|\frac{\varphi(V(m)) - \varphi(V(m)+0.001)}{0.001}\right|} + 0.001. \quad (25)$$

Fig. 14 shows the weight for each discrete voltage value.

Algorithm 3 WLS Solution to Match Standing Wave Amplitudes With Voltage Curve

1: Calculate $\phi(m)$ using (17), $m = 0, 1, \ldots, M-1$
2: Calculate $V(m)$ using (19), $m = 0, 1, \ldots, M-1$
3: Calculate weights $\alpha(m)$ for each of the $V(m)$ values using the modified derivatives from (25)
4: **repeat**
5:     Calculate W using (27)
6:     Calculate $w(m)$ using W and (20)
7:     **if** $\min(w(m)) < -15V$ **then**
8:         $\alpha(m) \leftarrow \alpha(m) \times 2$ at m at m where $w(m) = \min(w(m))$
9:         $V(m) \leftarrow V(m) + 0.005$ at m where $w(m) = \min w(m)$
10:     **else**
11:         **if** $\max(w(m)) > -4V$ **then**
12:             $\alpha(m) \leftarrow \alpha(m) \times 2$ at m where $w(m) = \max(w(m))$
13:             $V(m) \leftarrow V(m) - 0.005$ at m where $w(m) = \max w(m)$
14:         **end if**
15:     **end if**
16: **until** $w(m)$ has no elements outside the range $[-15V, -4V]$

With the weighting $\alpha(m)$ designed above, the Weighted LS (WLS) becomes

$$\min_{W} J = \min_{W} \sum_{m=0}^{M-1} \alpha(m) ||w(m) - V(m)||_2^2, \quad (26)$$

with the solution

$$\left(\sum_{m=0}^{M-1} \alpha(m) s_m s_m^T\right)^{-1} \left(\sum_{m=0}^{M-1} \alpha(m)(V(m) - W_0)s_m\right). \quad (27)$$

Since the WLS algorithm involves an $N \times N$ matrix inversion, and assuming the worst-case scenario where the inversion has to be repeated M times to satisfy the boundary conditions, its complexity is approximately bounded by $\mathcal{O}(MN^3)$, if the inversion is carried by Gauss-Jordan elimination. However, there exist more efficient algorithms to perform matrix inversion that result in lower complexity [22].

The simulations were repeated for the same scenario as in Section V-D2 using the WLS approach, which is outlined in Algorithm 3. It is possible that the WLS solution will result in voltage values that exceed the −15V and −4V boundaries. Therefore, Algorithm 3 provides additional steps that tighten the voltage boundaries every time this happens while increasing the weights associated with the element locations where the boundaries are violated. The W vector is calculated repeatedly until a solution is found that satisfies the original boundaries. The results shown in Fig. 15 demonstrate much smoother voltage and phase
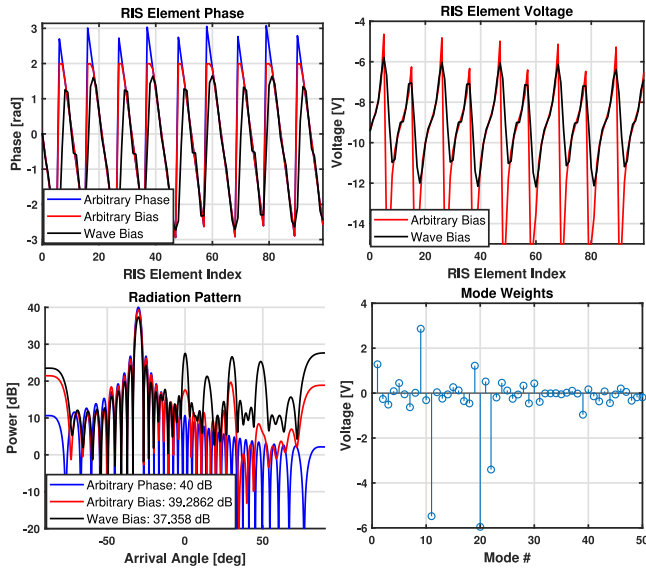
FIGURE 15. Maximizing SNR towards single receiver at −30° with WLS approach.

curves and an improved beampattern with around 1.9 dB loss in beamforming gain compared with the ideal case.

E. COMPARISONS OF THE TWO APPROACHES FOR OPTIMIZATION PROBLEM 1

The two varactor biasing configurations yield different performance for the case of maximizing SNR towards a single receiver direction. The main differences are in terms of the time required for convergence and the power reflected towards the desired direction. Simulation results for both approaches are compared in Table 2 for a case with $M = 100$ RIS elements, $N = 50$ modes and transmission lines extended $2d_x$ on the left and $2d_x$ on the right. The Weight Ranking and Brute Force algorithms were implemented for the envelope detector model, while the WLS algorithm was implemented for the SH model. All simulations assume normal incidence to the RIS surface with carrier frequency $f_c = 3$ GHz and standing wave $f_b = 12.9$ MHz. Note that the simulation times also include the time the program has to calculate the voltage waveforms and corresponding SNR values during optimization.

The results demonstrate that the WLS optimization yields superior results compared to the Weight Ranking and Brute Force algorithms. Although all algorithms perform well in steering power towards the desired receiver, the WLS approach is faster by orders of magnitude. Another weakness of the envelope detector model is its creation of a "ghost" peak in the negative of the desired direction, which can be avoided by making the transmission line much longer and eliminating the symmetry of the standing waves where varactors are present, as seen previously in Fig. 11. On the contrary, the WLS approach does not share this artificial symmetry, as seen in Fig. 15. Based on these results, we see that the SH model can be optimized much more efficiently and create a more accurate radiation pattern. Moreover, as

demonstrated in the next section, the WLS approach is very effective for the problem of optimizing for the SLNR when both beams and nulls must be created.

F. OPTIMIZATION PROBLEM 2: MAXIMIZING SIGNAL-TO-LEAKAGE-PLUS-NOISE RATIO AT MULTIPLE UE DIRECTIONS

As discussed previously, the SLNR problem is defined by (16), repeated here

$$\max_{\boldsymbol{\eta}} \text{SLNR} = \max_{\boldsymbol{\eta}} \frac{\min_{i \in \{1,2,...,K\}} \rho_s |\boldsymbol{h}_{d,i}^T \boldsymbol{\Phi} \boldsymbol{g}|^2}{\max_{j \in \{1,2,...,L\}} \rho_s |\boldsymbol{h}_{e,j}^T \boldsymbol{\Phi} \boldsymbol{g}|^2 + \sigma_s^2}.$$

The goal is to maximize the power reflected towards all K intended receiver directions, while minimizing the power reflected towards all L undesired receiver directions (either minimizing eavesdropping or reducing unwanted interference). The optimization metric is defined by the ratio of the minimum power directed towards a desired receiver and the maximum power steered towards an undesired direction with additive noise.

For this task, the Weight Ranking and Brute Force algorithms are not directly applicable, due to the difficulty in computing gradients for (16). Instead, we develop an alternative algorithm based on Simulated Annealing that will be discussed further in Section V-F2. Afterwards, simpler analytical algorithms that can be employed using the SH circuit model based on WLS optimization will be discussed as well. Before discussing the Simulated Annealing approach, it is necessary to discuss an important feature about the relationship between the standing waves and the corresponding radiation pattern of the RIS. Since Simulated Annealing requires random searches from a specific starting point, it is crucial to determine the best initialization for faster and more accurate convergence, similar to how the Weight Ranking algorithm provides an initial order for tuning the modes one-by-one. However, the approach presented below for Simulated Annealing is more intuitive and analytical, and results in a much simpler method for initializing the weights for further optimization.

1) CORRELATION BETWEEN MODAL FREQUENCIES AND PEAKS IN THE RADIATION PATTERN

As discussed above, further investigation of the relationship between the individual modes and the radiation pattern generated by the RIS is required to derive a more efficient optimization algorithm. Referring back to Fig. 10, it was demonstrated that a single sinusoid can produce two peaks at $\pm\theta^*$ in the radiation pattern for the envelope detector model. This is the result of the phase shift gradient across the RIS that collectively reflects a beam towards a specific direction [23]. If the phase gradient is steeper, corresponding to a sinusoid with higher frequency, the absolute value of the reflection angle increases. The same effect was seen in the sample-and-hold model. The expression for the mode

TABLE 2. Performance comparisons between SNR maximization for envelope detector vs. sample-and-hold models.

Rx Dir.	Envelope Detector		Sample and Hold	
θ^*	Power Steered	Optimization Time	Power Steered	Optimization Time
$-10°$	35.9418 dB	209.261 s	39.0365 dB	0.361 s
$-30°$	35.6064 dB	198.845 s	37.3580 dB	0.369 s
$-45°$	35.6419 dB	180.316 s	35.0566 dB	0.380 s
$-60°$	35.4927 dB	183.326 s	34.7838 dB	0.365 s
$-72°$	35.5045 dB	204.159 s	34.6151 dB	0.348 s
$24°$	35.4088 dB	162.451 s	37.9390 dB	0.333 s

number n that generates peaks at $\pm\theta^*$ for the sample-and-hold model is given by

$$n_{S/H} = \lfloor |2(M+1)\Delta \sin(\theta^*)| \rceil, \qquad (28)$$

where M is the number of RIS elements, Δ is the distance in wavelengths between the RIS elements, and n is rounded to the nearest integer value via the function $\lfloor . \rceil$ since the standing-wave modes are discrete. This formula also suggests that the spatial frequency corresponding to n is the minimal mode frequency required to generate a peak at θ^*. The derivation is provided in Appendix B.

A slightly different model holds for the envelope detector model. The transmission line assumed in our model in [8] is terminated by a short circuit. Therefore, the voltage reflection coefficient at the end of the transmission line is $\Gamma = -1$, and the reflected wave is inverted at the boundary [24]. Thus, each point on the transmission line experiences peaks due to both the positive and the negative traveling waves, and thus samples twice the number of peaks since it samples absolute values. Therefore, for a standing wave oscillating at frequency f, the peak detector will sample a peak at frequency $2f$, and the expression for the mode index n_{PD} that corresponds to the peak at θ^* will be

$$n_{PD} = \frac{n_{S/H}}{2}. \qquad (29)$$

This provides intuition for initializing which weights should be optimized in the Simulated Annealing approach described next.

2) MODE AMPLITUDE OPTIMIZATION USING SIMULATED ANNEALING

When optimizing a non-convex objective over a large number of variables, many algorithms tend to settle on local minima that may be far from the global optimum [25]. Particularly when using hill-climber methods such as the previously described combination of Weight Ranking and Brute Force search, the solution for the weights is highly dependent on the initialization, as well as the order in which the weights are being solved for. To address this issue, we use the Simulated Annealing approach described below.

Simulated Annealing (SA) is a stochastic optimization method that employs randomization to increase the likelihood of convergence to the global optimum. SA relies on the principle of "annealing" from physics, where a solid is cooled until it reaches its minimal energy state [26]. SA

uses Boltzmann distributions to find the probability of a state based on its temperature $T > 0$ and energy $f(x)$. The algorithm works as follows: Start with an initial system state and temperature. As the system matures, iteratively experiencing random updates that bring it towards a better or worse state with some probability that depends on the energy and temperature, the temperature decreases and approaches zero. As this happens, the system becomes less likely to randomly jump to worse states and converges towards a nearby minimum by moving in the direction that decreases its energy, which serves as the cost function [27].

To implement SA for the SLNR optimization problem, assume a set of K angles towards which the power gain should be maximized: $\theta^*_{arr} = [\theta^*_{d,1}, \theta^*_{d,2}, \ldots, \theta^*_{d,K}]$, and L angles towards which the reflected beam should be minimized. Define the vector $\boldsymbol{W}$ representing the mode amplitudes as the "state" of the system, and SLNR and SLNR_{new} as the "energy" of the system before and after a state update, respectively. Define the probability of switching to the next state as

$$p = \begin{cases} 1 & \text{SLNR}_{new} > \text{SLNR} \\ e^{\left(-\frac{\text{SLNR}-\text{SLNR}_{new}}{k_c T}\right)} & \text{SLNR}_{new} \leq \text{SLNR}. \end{cases} \qquad (30)$$

Let T denote the "temperature" based on the current iteration of the algorithm and k_c a constant representing the "cooling factor." The initial state vector $\boldsymbol{W}$ is excited only at specific modes corresponding to the peak directions determined by (28), with amplitudes set to $3/K$. This initializes the algorithm to a good starting point, while allowing for enough margin to update all the mode amplitudes as the algorithm progresses without saturating the voltage limits. The next state $\boldsymbol{W}_{new}$ is determined by adding a Gaussian random variable ϵ drawn from $\mathcal{N}(0,1)$ and scaled by a factor λ to each of the amplitudes in the state vector $\boldsymbol{W}$. The updated DC voltages $w(m)$ at each RIS element are calculated. If the SLNR_{new} of the new state is better than the current SLNR, then the algorithm chooses the better amplitude state. If it is worse, the algorithm will only update to that state if a random sample from a uniform distribution on the interval $(0, 1)$ is less than p, otherwise it will remain in the current state. Additionally, if the system remains in a worse state for longer than some upper limit of iterations, it will return to its previous best state $\boldsymbol{W}_{best}$ corresponding to SLNR_{best} and continue from there. The details of our SA implementation are given in Algorithm 4. The complexity of this algorithm
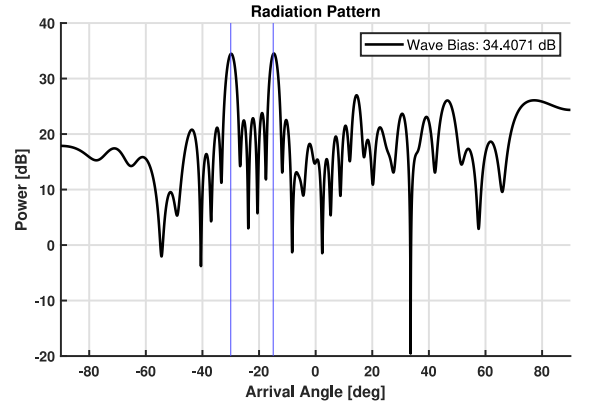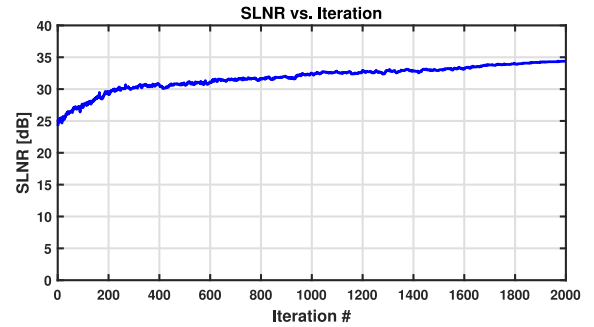
Algorithm 4 Simulated Annealing

1: $W \leftarrow [0, 0, \ldots, 0]^T$
2: Calculate indices n_k of each peak in θ^*_{arr}, using (28)
3: Each $W(n_k) \leftarrow \frac{3}{K}$
4: $\text{SLNR}_{best} \leftarrow -\infty$
5: $W_{best} \leftarrow W$
6: $i_{best} \leftarrow 0$
7: Calculate initial $w(m)$ using W and (20), $m = 0, \ldots, M - 1$
8: Calculate SLNR [dB] using $w(m)$ and (16)
9: **for** $i \in \{1, 2, \ldots, i_{max}\}$ **do**
10:     **if** $i - i_{best} \geq 100$ **then**
11:         $W \leftarrow W_{best}$
12:         $i_{best} \leftarrow i$
13:         $\text{SLNR} \leftarrow \text{SLNR}_{best}$
14:     **end if**
15:     $T \leftarrow 100\left(1 - \frac{i}{i_{max}}\right)$
16:     $W_{new}(n) \leftarrow W(n) + \lambda\epsilon, \quad \epsilon \sim \mathcal{N}(0, 1), \quad n = 1, 2, \ldots, N$
17:     Calculate $w(m)$ using W_{new} and (20), $m = 0, \ldots, M - 1$
18:     **if** $w(m)$ has elements outside $[-15V, -4V]$ **then**
19:         Increment i, go to step 10
20:     **end if**
21:     Calculate SLNR_{new} using $w(m)$ and (16)
22:     **if** $\text{SLNR}_{new} > \text{SLNR}_{best}$ **then**
23:         $\text{SLNR}_{best} \leftarrow \text{SLNR}_{new}$
24:         $W \leftarrow W_{new}$
25:         $W_{best} \leftarrow W$
26:         $i_{best} \leftarrow i$
27:     **else**
28:         Calculate p using (30)
29:         **if** $p \geq \text{rand}(1)$ **then**
30:             $W \leftarrow W_{new}$
31:             $\text{SLNR} \leftarrow \text{SLNR}_{new}$
32:         **end if**
33:     **end if**
34: **end for**

(a) Radiation Pattern, SLNR = 34.41 dB

(b) SLNR at every iteration of SA

FIGURE 16. Simulation results using SA for the sample-and-hold model, with desired receivers at $-30°$ and $-15°$ and no undesired receivers.

is $\mathcal{O}(i_{max}(M + N))$ since at each iteration, all N modes in W are updated and all M RIS elements are checked for boundary violations.

In our simulations, the SA algorithm was implemented with $\lambda = 0.03$, cooling factor $k_c = 0.002$, maximum number of iterations $i_{max} = 2000$. For the example in Fig. 16, two beams at -30° and -15° are desired assuming $M = 100$ RIS elements and $N = 50$ modes, with the transmission line extended by $2d_x$ before and after the first and last varactor ($M_l = M_r = 2$). The sample-and-hold circuit model was used for this example. The SA algorithm was able to increase the gain by almost 10 dB from the initialization point and achieves strong beams in the desired receiver directions, without reflections towards 15° and 30°. Fig. 17 shows the results for the same case as in Fig. 16, except that a desired

null is added at 20°. The SA algorithm improves the SLNR by around 25 dB and provides a deep null towards 20°, albeit at the cost of higher sidelobes in other directions.

We next applied the SA algorithm for the case of the envelope detector model with $W_0 = -4V$ and $w(m)$ calculated according to (11). The same simulation parameters were used as in the previous case, except that initial mode indices n_k were calculated instead using (29). The simulation results are shown in Fig. 18 and Fig. 19. We see that in both cases, the SA algorithm provides a significant boost in SLNR of approximately 6 dB and 20 dB, and is able to form deep nulls in directions close to the main beams. As in previous examples, the envelope detector architecture produces higher sidelobes and a strong beam in the broadside direction, unlike the sample-and-hold approach.

In the next section we focus on heuristic approaches for designing the RIS response to simultaneously steer beams and nulls in certain directions.

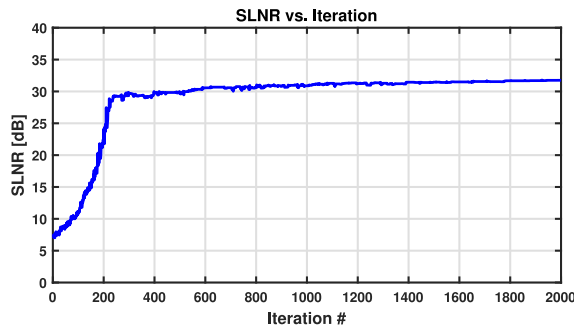### 3) MAXIMIZING POWER TOWARDS MULTIPLE RECEIVER DIRECTIONS ANALYTICALLY

We begin with the problem of maximizing the power steered towards multiple receiver directions, without any nulls:

$$\max_{\boldsymbol{\eta}} \min_{i \in \{1, 2, \ldots, K\}} \rho_s |\boldsymbol{h}_{d,i}^T \boldsymbol{\Phi} \boldsymbol{g}|^2. \tag{31}$$
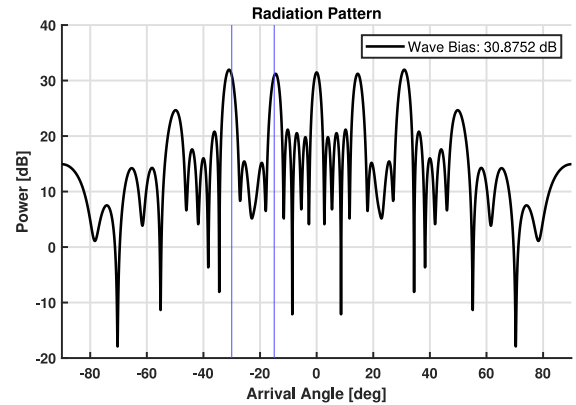
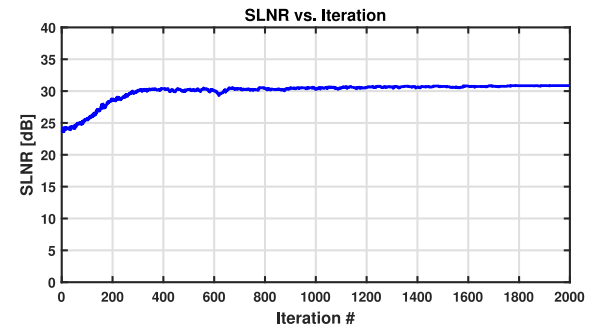While even this simpler problem cannot be solved analytically for our two circuit models, an approximate solution
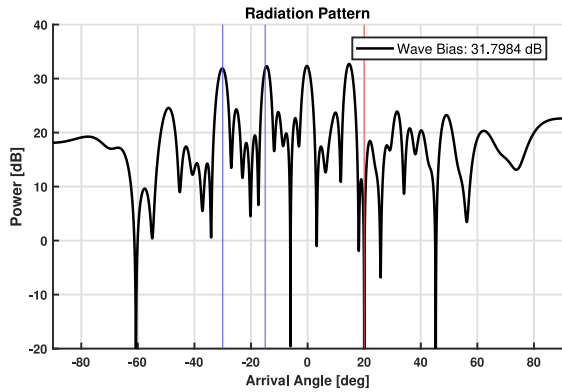
(a) Radiation Pattern, SLNR = 31.80 dB

(b) SLNR at every iteration of SA

FIGURE 17. Simulation results using SA for the sample-and-hold model, with desired receivers at −30° and −15° and undesired receiver at 20°.

(a) Radiation Pattern, SLNR = 30.88 dB

(b) SLNR at every iteration of SA

FIGURE 18. Simulation results using SA for the envelope detector model, with desired receivers at −30° and −15° and no undesired receivers.

can be found in a straightforward way, as discussed below for the three different parameterizations for η.

Ideal Phase – Here we use (17) to find the optimal set of reflection coefficients for each individual receiver direction $\theta_{d,i}^*$ for $i = 1, 2, \ldots, K$. We refer to each of these RIS phase configurations as $\phi_{d,i}(m)$ for $m = 0, 1, \ldots, M - 1$. Then, for each m, we take the average value of the reflection coefficients (which are complex), and we find the average over the K solutions

$$\phi(m) = \frac{1}{K} \sum_{i=1}^{K} \phi_{d,i}(m). \tag{32}$$

To satisfy the unit amplitude constraint after the averaging, we simply keep just the phase of the result: $\phi(m) \leftarrow \exp(j\angle\phi(m))$.

Arbitrary Voltage Bias – As in Section V-B2, we take the ideal reflection coefficients calculated above and map them to voltage values using (19), ensuring that the phase values remain within the boundaries allowed by the varactor biasing voltage.

Wave-Controlled Bias – We calculate the voltages of the modal decomposition using the WLS algorithm in Section V-D3.

Taking the average of the reflection coefficients will in general ensure that all receivers receive approximately the same amount of power. Some simulation results confirming

the effectiveness of the above approach are shown in Fig. 20 and 21. We see that the simple averaging approach provides beams in the desired directions, while using the arbitrary voltage bias reduces the power by only about 1 dB, and the standing wave bias by another 1–3 dB. The next section considers the problem of simultaneous null- and beamsteering.
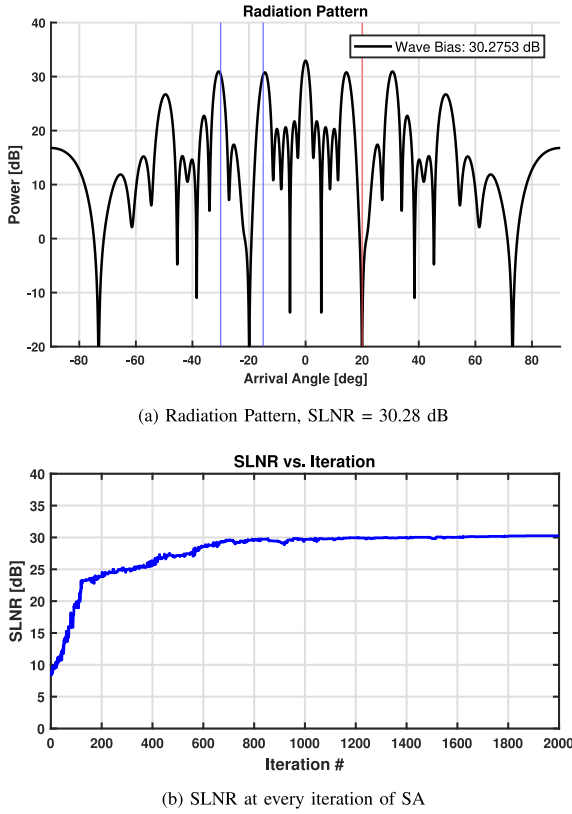
4) SIMULTANEOUS BEAM- AND NULL-STEERING

To form a null in a given direction $\theta_{e,j}^*$, the RIS configuration should satisfy

$$\sum_{m=0}^{M-1} \phi(m) e^{-jm\kappa\left(\theta_{e,j}^*\right)} \approx 0. \tag{33}$$

We propose a heuristic iterative approach that takes the solution from the previous section for the desired beams, and modifies it to add the nulls. The required steps are outlined in Algorithm 5 for the ideal phase case. The algorithm starts by calculating the reflection coefficients required to form beams at the desired directions. Then, it iteratively tunes the reflection coefficients by calculating their product with the channel coefficients that correspond to each null direction $\theta_{e,j}^*$,

$$r_j(m) = \phi(m) e^{-jm\kappa\left(\theta_{e,j}^*\right)}, \tag{34}$$
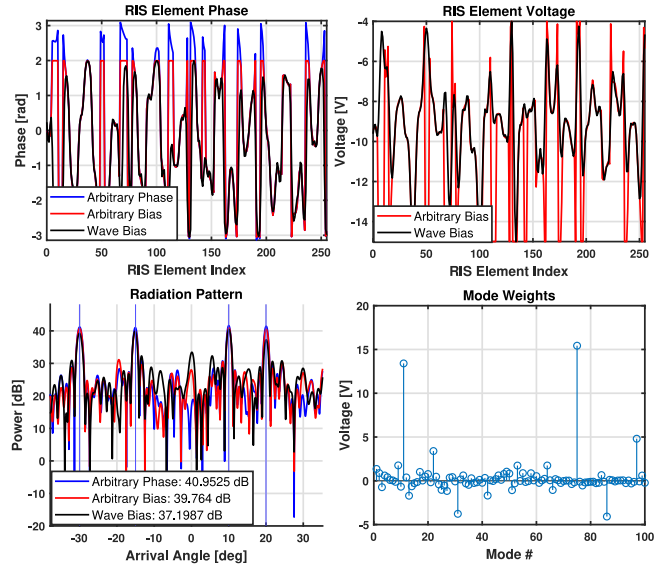
(a) Radiation Pattern, SLNR = 30.28 dB

(b) SLNR at every iteration of SA

FIGURE 19. Simulation results using SA for the envelope detector model, with desired receivers at −30° and −15° and an undesired receiver at 20°.
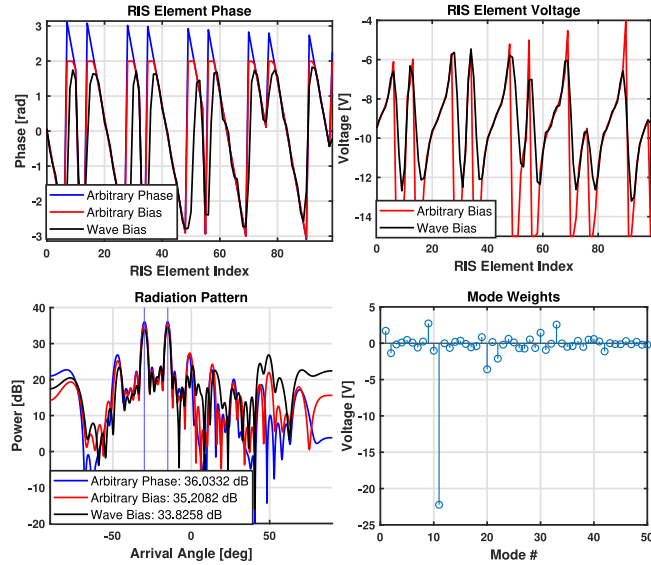
FIGURE 20. Maximizing power reflected towards two directions using the sample-and-hold model. $M = 100$ RIS elements, $N = 50$ modes, $M_l = M_r = 2$. Desired beams at −30° and −15°.

FIGURE 21. Maximizing power reflected towards four directions using sample-and-hold model. $M = 256$ RIS elements, $N = 100$ modes, $M_l = M_r = 2$. Desired beams at −30°, -15°, 10°, and 20°.

Algorithm 5 RIS Design for Simultaneous Beam and Null Steering

---

1: **for** each desired beam direction $\theta_{d,i}^*$ **do**
2:     Calculate $\phi_{d,i}(m)$ using (17), $\quad i = 1, \ldots, K$.
3: **end for**
4: $\phi(m) \leftarrow \frac{1}{K} \sum_{i=1}^{K} \phi_{d,i}(m)$.
5: $\phi(m) \leftarrow \exp(j\underline{/\phi(m)})$.
6: **repeat**
7:     **for** each null direction $\theta_{e,j}^*$ **do**
8:         $r_j(m) \leftarrow \phi(m)e^{-jm\kappa(\theta_{e,j}^*)}$, $m = 0, \ldots, M-1$.
9:         Calculate $\bar{r}_j = \frac{1}{M} \sum_{m=0}^{M-1} r_j(m)$.
10:         $\phi(m) \leftarrow \left(\frac{r_j(m) - \bar{r}_j}{e^{-jm\kappa(\theta_{e,j}^*)}} \right)$, $m = 0, \ldots, M-1$.
11:         $\phi(m) \leftarrow \exp(j\underline{/\phi(m)})$, $m = 0, \ldots, M-1$.
12:     **end for**
13: **until** $\max(|\bar{r}_1|, \bar{r}_2, \ldots, |\bar{r}_L|) \leq \mu$.

---

as outlined in steps 10 and 11 of Algorithm 5. The same procedure is repeated until the response of the RIS is orthogonalized towards all eavesdropper directions and the power gains at those directions are below some threshold μ. The complexity of the first loop in the algorithm, which calculates the reflection phases for all K desired beam directions, is $\mathcal{O}(KM)$. The complexity of the second loop is $\mathcal{O}(TLM)$, where L is the number of null directions and T is the worst-case estimate for the number of times the reflection coefficients must be averaged, which depends on the threshold μ. The complexity of the algorithms proposed in this paper are compared in Table 3.

The same approach can be used for the arbitrary voltage case, except that the reflection phase values are converted to voltages and vice versa between iterations to account for the limited phase values. Since the changes in the phase and

calculating the average value $\bar{r}_j$, and subtracting the average from each $r_j(m)$ to make their new average zero. At this point, (33) is satisfied and the updated reflection coefficients are mapped back into $\phi(m)$ by dividing the result by the channel coefficients and using the phase of the new result,

TABLE 3. Complexity of the proposed algorithms for tuning the wave-controlled RIS.

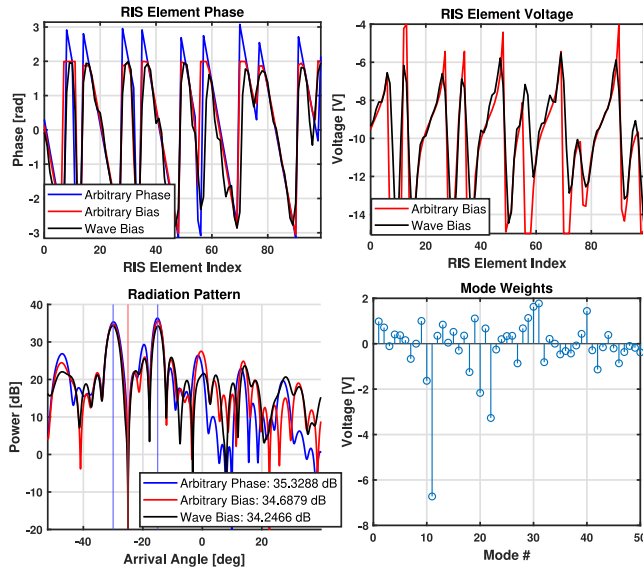| Algorithm	Complexity
Weight Ranking	$\mathcal{O}(kN + N\log N)$
Brute Force	$\mathcal{O}(MN\log\frac{1}{\mu_f})$
Weighted Least Squares	$\mathcal{O}(MN^3)$
Simulated Annealing	$\mathcal{O}(i_{max}(M+N))$
RIS Design for Simultaneous Beam and Null Steering	$\mathcal{O}((K+TL)M)$

FIGURE 22. Simultaneous beam- and null-steering using the sample-and-hold model with $M = 100$ RIS elements, $N = 50$ modes, $M_l = M_r = 2$. Desired beams at $-30°$ and $-15°$ and one null at $-25°$.

voltage curves are so slight, the WLS algorithm has trouble forming the nulls for the wave-controlled case. Thus, it fails to match the SLNR values simply by attempting to match the ideal voltage and phase curves with the wave-controlled ones. For the final touches, we define the *Combined Algorithm* – Start with Algorithm 5 to find the initial reflection phases. Then, map those phase values into voltage values using (19) and convert those to mode amplitudes using WLS. Finally, increase the SLNR and form deep nulls using SA.

Simulation results showing the performance of the above Combined Algorithm are given in Figs. 22 and 23. We see that this algorithm implemented for the wave-controlled approach has less than 1 dB of loss in SLNR compared with the use of arbitrary biasing voltages for both cases. The beampatterns show strong peaks in the desired directions (blue vertical lines) and deep nulls in the undesired directions (red vertical lines).

5) SLNR GAIN FOR VARIOUS NUMBERS OF ELEMENTS AND MODES

In this section, using the Combined Algorithm, we compare the performance of the proposed waveguide RIS for different numbers of RIS elements and standing-wave modes, using the sample-and-hold circuit realization. For the first scenario, we study performance versus the number of modes N, where in this case we use the first N modes in the decomposition. The case considered is the same as in Fig. 23, with four
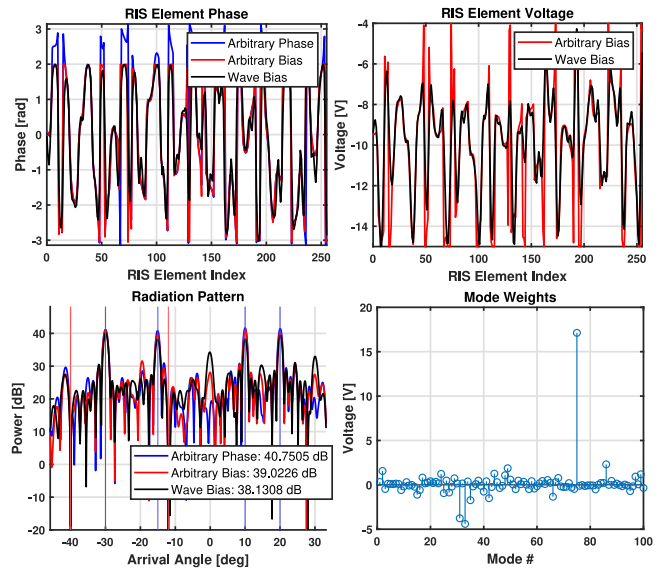

FIGURE 23. Simultaneous beam- and null-steering using the sample-and-hold model with $M = 256$ RIS elements, $N = 100$ modes, $M_l = M_r = 2$. Desired beams at $-30°$, $-15°$, $10°$, and $20°$, and nulls at $-40°$ and $-12°$.
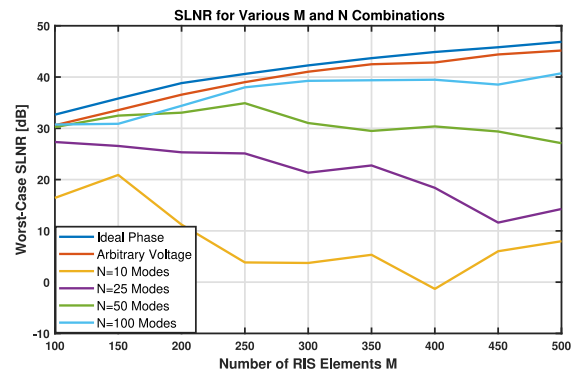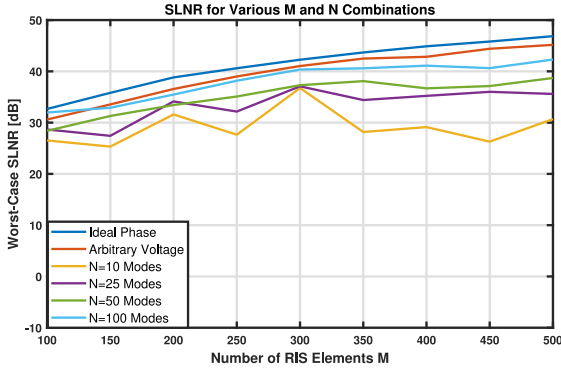

FIGURE 24. Worst-case SLNR for various numbers of RIS elements and modes with the sample-and-hold circuit. There are desired beams at $-30°$, $-15°$, $10°$ and $20°$, and nulls at $-12°$ and $-40°$. Each data point is the result of optimization using the Combined Algorithm, averaged over 10 trials.

desired beams at $-15°$, $-30°$, $10°$, and $20°$, and two nulls at $-12°$ and $-40°$. All RIS configurations are assumed to have a transmission line extended by $2d_x$ both on the left and right ($M_l = M_r = 2$). The performance of the different RIS designs is plotted in Fig. 24.

It is observed that the SLNR performance of the ideal phase and arbitrary voltage cases grow steadily with the number of RIS elements. Interestingly, the SLNR for the wave-controlled approach only increases with M when N is large. This is due to the fact that we are using only the first N harmonics. Small values of N mean that the modes cover a relatively small and decreasing set of frequencies as M grows. This is clear from the results in Fig. 25 for the same scenario, except in this case we choose the N strongest modes to construct the wave-controlled biasing. Here we see that relatively few modes are needed to nearly match the performance achievable with arbitrary phase control. We also observe that increases in the number of modes past a certain

FIGURE 25. Worst-case SLNR for various numbers of RIS elements and modes with the sample-and-hold circuit, where only the modes with the strongest amplitudes are selected. There are desired beams at −30°, −15°, 10° and 20°, and nulls at −12° and −40°. Each data point is the result of optimization using the Combined Algorithm, averaged over 10 trials.

point provides a relatively marginal benefit. In general, in a traditional RIS scheme, as the size of the RIS increases, the hardware required for the control becomes more complex. Although this holds true for any RIS implementation, our approach shows steady performance using fewer degrees of freedom and thus, the amount of overhead required to control the RIS does not necessarily scale with the size of the RIS.

Although the examples in this research use the assumption of normal incidence and a line-of-sight beam reflection, the algorithms discussed in this section may be generalized to other cost functions. If the channel characteristics are known, an analytical solution using the Combined Algorithm for a specific metric (such as increasing power at a specific direction) may be employed. Otherwise, a feedback loop between the receiver and the RIS controller may be used in conjunction with SA to optimize the response of the RIS based on the cost function defined.

VI. CONCLUSION

This paper has presented implementation aspects associated with an RIS architecture in which the varactor biasing voltages are supplied by standing waves on a transmission line. The standing wave is created by a waveform generator that can control the amplitude of a number of harmonically related sinusoidal modes injected at one end of the transmission line. Such an architecture significantly simplifies the wiring and circuitry required to control the RIS, and potentially reduces the amount of control information that must be sent for RIS configuration. Two methods of converting the AC standing waves to DC varactor biasing voltages have been studied: an envelope detector and a sample-and-hold circuit. Based on models for these circuits, algorithms for optimizing the mode amplitudes have been developed to design radiation patterns with desired beam- and null-steering. While the envelope detector circuit is simpler to implement, optimization of the mode amplitudes is significantly more complicated and provides performance that is inferior to the sample-and-hold architecture. Simulations of the system performance demonstrate the ability of the

wave-controlled RIS to generate strong beams and deep nulls in desired directions, with a relatively small degradation in terms of SNR or SLNR compared with the case of arbitrary control of each varactor element and idealized RIS models in which the RIS phase response can be arbitrarily specified.

APPENDIX A
DERIVATION OF LS RESULTS

We wish to replicate an arbitrary voltage waveform $V(m)$ for all $m = 0, 1, \ldots, M - 1$ using N sinusoids that construct the waveform $w(m)$ as in (20) and using DC voltage bias W_0 given by (21). The variable $w(m)$ can be re-written as

$$w(m) = W_0 + \boldsymbol{W}^T \boldsymbol{s}_m \tag{35}$$

where $\boldsymbol{W} = [W_1, W_2, \ldots, W_N]^T$ is the vector representing all the mode weights, and

$$\boldsymbol{s}_m = \left[\sin\left(\frac{\pi(m + M_l)}{M - 1 + M_l + M_r}\right) \sin(\omega_b t_0), \ldots, \right.$$
$$\left. \sin\left(\frac{N\pi(m + M_l)}{M - 1 + M_l + M_r}\right) \sin(N\omega_b t_0) \right]^T$$

is the vector containing all the sinusoid terms before they are multiplied by each mode weight, at any RIS element m. Define the cost function to minimize as

$$J = \sum_{m=0}^{M-1} ||w(m) - V(m)||_2^2. \tag{36}$$

Expanding, we have

$$\min_{\boldsymbol{W}} J = \min_{\boldsymbol{W}} \sum_{m=0}^{M-1} \left(V^2(m) - 2V(m)w(m) + w^2(m) \right). \tag{37}$$

To minimize the cost function, take its gradient or vector derivative and set it equal to the zero vector

$$\frac{\partial J}{\partial \boldsymbol{W}} = \sum_{m=0}^{M-1} \left(-2V(m)\frac{\partial w(m)}{\partial \boldsymbol{W}} + 2w(m)\frac{\partial w(m)}{\partial \boldsymbol{W}} \right) = 0 \tag{38}$$

where we use the notation $\frac{\partial J}{\partial \boldsymbol{W}}$ to mean the gradient of J with respect to the vector $\boldsymbol{W}$. The partial derivative of $w(m)$ with respect to $\boldsymbol{W}$ is

$$\frac{\partial w(m)}{\partial \boldsymbol{W}} = \boldsymbol{s}_m. \tag{39}$$

Plugging back, we get

$$\frac{\partial J}{\partial \boldsymbol{W}} = \sum_{m=0}^{M-1} \left(-2V(m)\boldsymbol{s}_m + 2\left[W_0 + \boldsymbol{W}^T \boldsymbol{s}_m \right]\boldsymbol{s}_m \right) = 0. \tag{40}$$

Since $\boldsymbol{W}^T \boldsymbol{s}_m$ is a constant, it is equivalent to its transpose $\boldsymbol{s}_m^T \boldsymbol{W}$. Also, vectors can be multiplied by constants from either side, therefore $\boldsymbol{W}^T \boldsymbol{s}_m \boldsymbol{s}_m = \boldsymbol{s}_m \boldsymbol{s}_m^T \boldsymbol{W}$, and

$$2 \sum_{m=0}^{M-1} \boldsymbol{s}_m \boldsymbol{s}_m^T \boldsymbol{W} = 2 \sum_{m=0}^{M-1} (V(m) - W_0)\boldsymbol{s}_m. \tag{41}$$

Solving for optimal W yields

$$W = \left(\sum_{m=0}^{M-1} s_m s_m^T\right)^{-1} \left(\sum_{m=0}^{M-1} (V(m) - W_0)s_m\right). \quad (42)$$

This expression will yield the minimum of the cost function due to the positive definite nature of the $\sum_{m=0}^{M-1} s_m s_m^T$ matrix, which also allows its inversion [28]. ∎

Theorem: The s_m vectors are linearly independent, immediately implying that the matrix sum $\sum_{m=0}^{M-1} s_m s_m^T$ is positive definite.

Proof: To prove that $\sum_{m=0}^{M-1} s_m s_m^T$ is positive definite, we will first prove, in items 1) and 2) below, that $\{s_m\}_{m=0}^{M-1}$ is a linearly independent set under the given conditions, and then, in item 3) below, we will prove that $\sum_{m=0}^{M-1} s_m s_m^T$ is positive definite.

1) Each s_m is generated using sinusoids of the form $\sin(\frac{n\pi(m+M_l)}{M-1+M_l+M_r})$, multiplied by weighting factors $\sin(n\omega_b t_0) \neq 0$ for every $n = 1, 2, \ldots, N$. Assume $M_l = 0$ and $M_r = 0$. Then, the maximum number of N for which $s_m \neq \mathbf{0}$ is $M - 2$ (due to the cases where $m = 0$ and $m = M - 1$, because $\sin(0) = \sin(\pi) = 0$). To get additional contributions from the edge cases for the LS solution, it is sufficient to have $M_l \geq 1$ and $M_r \geq 1$.

2) Since each s_m has sinusoidal components with frequencies dependent on m, each s_i is linearly independent from s_j where $i \neq j$. The proof is given below.

   Lemma: N signals are linearly independent in the time domain if and only if they are linearly independent in the frequency domain.

   Proof: The set of functions $\{g_i(t)\}_{i=1}^N$ is linearly independent on $(-\infty, \infty)$ if

$$\sum_{i=1}^N a_i g_i(t) = 0, \quad t \in (-\infty, \infty) \quad (43)$$

   implies $a_i = 0$ for $i = 1, 2, \ldots, N$ [29]. Assume there exist constants a_i for which $\sum_{i=1}^N a_i g_i(t) = 0$. Taking the Fourier transform results in

$$\mathscr{F}\left\{\sum_{i=1}^N a_i g_i(t)\right\} = \sum_{i=1}^N a_i \mathscr{F}\{g_i(t)\}$$
$$= \sum_{i=1}^N a_i G_i(f) = 0 \quad (44)$$

   since $\mathscr{F}\{0\} = 0$. In other words, the same set of a_i makes the linear combination in the frequency domain equal to zero. If the functions $g_i(t)$ all have different frequency components, they will all occupy separate sections in the frequency domain. Therefore, the summation of them will only amount to zero for $f \in (-\infty, \infty)$ if $a_i = 0$ for $i = 1, 2, \ldots, N$. This argument shows that linear independence in the time

domain implies linear independence in the frequency domain (sufficient condition). The necessary condition follows from the duality property of the Fourier transform. ∎

3) *Lemma:* If $\{s_m\}_{m=0}^{M-1}$ is a linearly independent set of vectors, then the matrix $\sum_{m=0}^{M-1} s_m s_m^T$ is positive definite.

   Proof: Assume $\sum_{m=0}^{M-1} s_m s_m^T$ is not positive definite. Then, there exists a vector w_0 such that $w_0^T(\sum_{m=0}^{M-1} s_m s_m^T)w_0$ is not greater than 0. Consider

$$w_0^T\left(\sum_{m=0}^{M-1} s_m s_m^T\right)w_0 = \sum_{m=0}^{M-1} w_0^T s_m s_m^T w_0,$$
$$= \sum_{m=0}^{M-1} \left(w_0^T s_m\right)^2. \quad (45)$$

The quantity in (45) is a sum of squares, therefore it cannot be less than zero. So, if $\sum_{m=0}^{M-1} s_m s_m^T$ is not positive definite, then $\sum_{m=0}^{M-1} (w_0^T s_m)^2 = 0$. This can only happen if $w_0^T s_m = 0$ for all $m = 0, 1, \ldots, M - 1$. But, that means s_m are all proportional, i.e.,

$$s_m = \beta_m s_0 \quad m = 0, 1, \ldots, M - 1,$$

where β_m is a constant. Which implies $\{s_m\}_{m=0}^{M-1}$ is not a linearly independent set. But that contradicts the hypothesis and the proof is complete. ∎

The summation of M such $(N \times N)$ matrices therefore results in a full rank matrix with nonzero eigenvalues, where $N \leq M - 2 + \min(M_l, 1) + \min(M_r, 1)$. Therefore, $\sum_{m=0}^{M-1} s_m s_m^T$ is positive definite and invertible. The matrix would remain positive definite also for the case $\sum_{m=0}^{M-1} \alpha(m)s_m s_m^T$ where $\alpha(m) > 0$, since these are just scaling factors that would not interfere with the number of positive eigenvalues in the overall summation matrix.

APPENDIX B
MAIN MODES CORRESPONDING TO SPECIFIC REFLECTION ANGLES

Let $W = [0, 0, \ldots, 0]^T$ be the $N \times 1$ zero vector containing all vanishing mode amplitudes, except for one index n. The resulting standing wave voltage at each element $m = 0, \ldots, M - 1$, is given by

$$w(m) = W_0 + W_n \sin\left(\frac{n\pi m}{M-1}\right)\sin(n\omega_b t_0)$$
$$= W_0 + C\sin\left(\frac{n\pi m}{M-1}\right). \quad (46)$$

This means that $w(m)$ oscillates with a spatial angular frequency $\kappa = \frac{n\pi}{M-1}$. This also suggests that the phase shift $\varphi(w(m))$ of the RIS reflection coefficient will also oscillate with that same spatial frequency since the conversion between voltage to phase is one-to-one (although it is nonlinear), for the frequencies of interests shown in Fig. 7.

While still maintaining the assumption that the amplitudes of the reflection coefficients are $|\phi(m)| \leq 1$, one can approximate

$$\angle\phi(m) \approx \phi_0 + D \sin\left(\frac{n\pi m}{M-1} + \alpha\right). \qquad (47)$$

Assume $\phi_0 = 0$, $\alpha = 0$, and $D = 1$ for simplicity. The power directed towards a specific receiver direction θ^* is calculated using the definitions from Section V-A,

$$P = \rho_s \left| \sum_{m=0}^{M-1} \phi(m) e^{-jm\kappa(\theta^*)} \right|^2. \qquad (48)$$

Applying Euler's identity to (47) and combining with the above definition gives

$$P \approx \rho_s \left| \sum_{m=0}^{M-1} \frac{1}{j2} \left[e^{\left(\frac{jn\pi m}{M-1}\right)} - e^{\left(-\frac{jn\pi m}{M-1}\right)} \right] e^{-jm\kappa(\theta^*)} \right|^2$$

$$= \rho_s \left| \frac{1}{2} \sum_{m=0}^{M-1} e^{\left[j\left(\frac{n\pi m}{M-1} - m\kappa(\theta^*)\right)\right]} - e^{\left[-j\left(\frac{n\pi m}{M-1} + m\kappa(\theta^*)\right)\right]} \right|^2. \qquad (49)$$

Since $n > 0$, only the first complex exponential term can become unity to maximize the power towards θ^*, thus

$$\frac{n\pi m}{M-1} = m\kappa(\theta^*). \qquad (50)$$

Without the case where $m = 0$, the index n that maximizes the power is

$$n = \frac{(M-1)\kappa(\theta^*)}{\pi}. \qquad (51)$$

Substituting $\kappa(\theta^*)$ as $2\pi\Delta\sin(\theta^*)$ in (51) and taking the absolute value since $n > 0$ results in

$$n = \left| \frac{2\pi\Delta(M-1)\sin(\theta^*)}{\pi} \right| = \left| 2(M-1)\Delta\sin(\theta^*) \right|, \qquad (52)$$

which can be rounded to the nearest integer value $\lfloor \cdot \rceil$.

REFERENCES

[1] C. Pan et al., "An overview of signal processing techniques for RIS/IRS-aided wireless systems," *IEEE J. Sel. Topics Signal Process.*, vol. 16, no. 5, pp. 883–917, Aug. 2022.

[2] A. Swindlehurst, G. Zhou, R. Liu, C. Pan, and M. Li, "Channel estimation with reconfigurable intelligent surfaces—A general framework," *Proc. IEEE*, vol. 110, no. 9, pp. 1312–1338, Sep. 2022.

[3] S. Xia, X. Chen, and H. Yin, "DFT based compression algorithm for configuration coefficients of reconfigurable intelligent surface," in *Proc. 13th Int. Conf. Wireless Commun. Signal Process. (WCSP)*, 2021, pp. 1–5.

[4] B. Sokal, P. R. B. Gomes, A. L. F. De Almeida, B. Makki, and G. Fodor, "Reducing the control overhead of intelligent reconfigurable surfaces via a tensor-based low-rank factorization approach," *IEEE Trans. Wireless Commun.*, vol. 22, no. 10, pp. 6578–6593, Oct. 2023.

[5] A. Sayanskiy et al., "A 2D-programmable and scalable reconfigurable intelligent surface remotely controlled via digital infrared code," *IEEE Trans. Antennas Propag.*, vol. 71, no. 1, pp. 570–580, Jan. 2023.

[6] S. Y. Miao and F. H. Lin, "Light-controlled large-scale wirelessly reconfigurable microstrip reflectarrays," *IEEE Trans. Antennas Propag.*, vol. 71, no. 2, pp. 1613–1622, Feb. 2023.

[7] T. Hershko, D. Rozban, G. Kedar, A. Etinger, and A. Abramovich, "Photodiode as tuning element for metasurface intelligent reflecting surface based on steer by image technology," in *Proc. IEEE Int. Symp. Antennas Propagat. INC/USNC-URSI Radio Sci. Meeting*, 2024, pp. 825–826.

[8] E. Ayanoglu, F. Capolino, and A. L. Swindlehurst, "Wave-controlled metasurface-based reconfigurable intelligent surfaces," *IEEE Wireless Commun.*, vol. 29, no. 4, pp. 86–92, Aug. 2022.

[9] T. Sleasman et al., "Waveguide-fed tunable metamaterial element for dynamic apertures," *IEEE Antennas Wireless Propag. Lett.*, vol. 15, pp. 606–609, 2016.

[10] N. Shlezinger, G. C. Alexandropoulos, M. F. Imani, Y. C. Eldar, and D. R. Smith, "Dynamic metasurface antennas for 6G extreme massive MIMO communications," *IEEE Wireless Commun.*, vol. 28, no. 2, pp. 106–113, Apr. 2021.

[11] D. Hanna, M. Saavedra-Melo, F. Shan, and F. Capolino, "A versatile polynomial model for reflection by a reflective intelligent surface with varactors," in *Proc. IEEE Int. Symp. Antennas Propagat. USNC-URSI Radio Sci. Meeting*, 2022, pp. 679–680.

[12] F. Costa and M. Borgese, "Electromagnetic model of reflective intelligent surfaces," *IEEE Open J. Commun. Soc.*, vol. 2, pp. 1577–1589, 2021.

[13] P. Nayeri, F. Yang, and A. Z. Elsherbeni, "Beam-scanning reflectarray antennas," in *Reflectarray Antennas: Theory, Designs, and Applications*. Hoboken, NJ, USA: Wiley, 2018, pp. 303–366.

[14] F. Capolino, A. Vallecchi, and M. Albani, "Equivalent transmission line model with a lumped X-circuit for a metalayer made of pairs of planar conductors," *IEEE Trans. Antennas Propag.*, vol. 61, no. 2, pp. 852–861, Feb. 2013.

[15] D. Sievenpiper, L. Zhang, R. F. J. Broas, N. G. Alexopolous, and E. Yablonovitch, "High-impedance electromagnetic surfaces with a forbidden frequency band," *IEEE Trans. Microw. Theory Techn.*, vol. 47, no. 11, pp. 2059–2074, Nov. 1999.

[16] S. R. Best and D. L. Hanna, "Design of a broadband dipole in close proximity to an EBG ground plane," *IEEE Antennas Propag. Mag.*, vol. 50, no. 6, pp. 52–64, Dec. 2008.

[17] M. Saavedra-Melo, K. Rouhi, and F. Capolino, "Wave-controlled RIS: A novel method for reconfigurable elements biasing," in *Proc. IEEE Int. Symp. Antennas Propagat. USNC-URSI Radio Sci. Meeting*, 2023, pp. 979–980.

[18] S. Haykin, *Communication Systems*, 3rd ed. Hoboken, NJ, USA: Wiley, 1994.

[19] P. Horowitz and W. Hill, *The Art of Electronics*. Cambridge, U.K.: Cambridge Univ. Press, 1980.

[20] I. Vardakis, G. Kotridis, S. Peppas, K. Skyvalakis, G. Vougioukas, and A. Bletsas, "Intelligently wireless batteryless RF-powered reconfigurable surface: Theory, implementation & limitations," *IEEE Trans. Wireless Commun.*, vol. 22, no. 6, pp. 3942–3954, Jun. 2023.

[21] S. Russell and P. Norvig, *Artificial Intelligence: A Modern Approach*, 4th ed. London, U.K.: Pearson, 2021.

[22] M. D. Petković and P. S. Stanimirović, "Generalized matrix inversion is not harder than matrix multiplication," *J. Comput. Appl. Math.*, vol. 230, no. 1, pp. 270–282, 2009. [Online]. Available: https://www.sciencedirect.com/science/article/pii/S0377042708006237

[23] Z. Mao, W. Wang, Q. Xia, C. Huang, X. Pan, and Z. Ye, "Amplitude-dependent phase-gradient directional beamforming for IRS: A scalable optimization framework," *IEEE Trans. Commun.*, vol. 72, no. 4, pp. 2354–2369, Apr. 2024.

[24] J. F. White, *High Frequency Techniques: An Introduction to RF and Microwave Design and Computer Simulation*. Hoboken, NJ, USA: Wiley, 2004.

[25] Y. Plan and R. Vershynin, "The generalized Lasso with non-linear observations," *IEEE Trans. Inf. Theory*, vol. 62, no. 3, pp. 1528–1537, Mar. 2016.

[26] V. Černý, "Thermodynamical approach to the traveling salesman problem: An efficient simulation algorithm," *J. Optim. Theory Appl.*, vol. 45, pp. 41–51, Jan. 1985.

[27] Z. Yahong, L. Cuiran, and L. Yongje, "Simulated annealing genetic algorithm based RIS phase optimization in the high-speed communication of the railways," in *Proc. 8th Int. Conf. Commun., Image Signal Process. (CCISP)*, 2023, pp. 1–5.

[28] A. Papoulis, *Probability, Random Variables, and Stochastic Processes*. New York, NY, USA: McGraw-Hill, 1965.

[29] G. Bachman and L. Narici, *Functional Analysis*, 2nd ed. Mineola, NY, USA: Dover Publ., 2000.
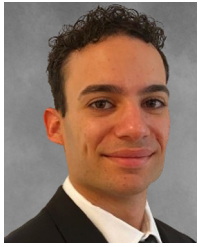
GAL BEN-ITZHAK (Graduate Student Member, IEEE) received the B.S. and M.S. degrees in electrical engineering from the University of California at Irvine, Irvine, CA, USA, in 2023 and 2024, respectively, where he is currently pursuing the Ph.D. degree. His current research and professional interests include high-speed communications, optimization, digital signal processing, high-speed circuit design, signal integrity, and power integrity.

MIGUEL SAAVEDRA-MELO (Graduate Student Member, IEEE) received the B.S. and M.S. degrees in electronic engineering from the Universidad Nacional de Colombia, Bogotá, Colombia, in 2014 and 2018, respectively. He is currently pursuing the Ph.D. degree in electrical engineering with the University of California at Irvine, Irvine, CA, USA. His current research interests include electron beam devices, reflective intelligent surfaces, and high-power microwaves.

BENJAMIN BRADSHAW (Graduate Student Member, IEEE) received the first B.S. degree in mathematics and the second B.S. degree in physics from Utah State University, Logan, UT, USA, in 2022. He is currently pursuing the Ph.D. degree in computational science with the University of California (UCI) at Irvine, Irvine, CA, USA. At UCI, his current research focus is in the field of RF engineering with reconfigurable intelligent surfaces.

ENDER AYANOGLU (Fellow, IEEE) received the Ph.D. degree in electrical engineering from Stanford University, Stanford, CA, USA, in 1986. He was with the Bell Laboratories Communications Systems Research Laboratory, Holmdel, NJ, USA. From 1999 to 2002, he was a Systems Architect with Cisco Systems Inc., San Jose, CA, USA. Since 2002, he has been a Professor with the Department of Electrical Engineering and Computer Science, University of California at Irvine, Irvine, CA, USA, where he was the Director of the Center for Pervasive Communications and Computing and the Conexant-Broadcom Endowed Chair from 2002 to 2010. He was a recipient of the IEEE Communications Society Stephen O. Rice Prize Paper Award in 1995, the IEEE Communications Society Best Tutorial Paper Award in 1997, and the IEEE Communications Society Communication Theory Technical Committee Outstanding Service Award in 2014. In 2023, he received the IEEE Communications Society Joseph L. LoCicero Award for outstanding contributions to IEEE Communications Society journals as an Editor, the Editor-in-Chief, and the founding EiC. From 2000 to 2001, he was the Founding Chair of the IEEE-ISTO Broadband Wireless Internet Forum, an industry standards organization. He served on the Executive Committee for the IEEE Communications Society Communication Theory Committee from 1990 to 2002, and its Chair from 1999 to 2002. From 1993 to 2014, he was an Editor of IEEE TRANSACTIONS ON COMMUNICATIONS. He was the Editor-in-Chief of IEEE TRANSACTIONS ON COMMUNICATIONS from 2004 to 2008, and the IEEE JOURNAL ON SELECTED AREAS IN COMMUNICATIONS Series on Green Communications and Networking from 2014 to 2016. He was the Founding Editor-in-Chief of IEEE TRANSACTIONS ON GREEN COMMUNICATIONS AND NETWORKING from 2016 to 2020. He served as an IEEE Communications Society Distinguished Lecturer from 2022 to 2023 and will serve in the same capacity in 2024 and 2025.

FILIPPO CAPOLINO (Fellow, IEEE) received the Laurea (cum laude) and Ph.D. degrees in electrical engineering from the University of Florence, Italy, in 1993 and 1997, respectively. From 1997 to 1999, he was a Fulbright and then a Postdoctoral Fellow with the Department of Aerospace and Mechanical Engineering, Boston University, MA, USA. From 2000 to 2001, part of 2005 and in 2006, he was a Research Assistant Visiting Professor with the Department of Electrical and Computer Engineering, University of Houston, TX, USA. From 2002 to 2008, he was an Assistant Professor with the Department of Information Engineering, University of Siena, Italy. He was a Visiting Professor with the Fresnel Institute, Marseille, France, in 2003, and with the Centre de Recherche Paul Pascal, Bordeaux, France, in 2010. He is currently a Professor with the Department of Electrical Engineering and Computer Science, University of California at Irvine, Irvine, CA, USA. In 2022, he held the title of Cathedra of Excellence with the University of Carlos III, Madrid, Spain. His current research interests include metamaterials and their applications, antennas and wireless systems, sensors in both microwave and optical ranges, millimeter wave technology, electron beam devices, plasmonics, microscopy, optical devices, and applied electromagnetics in general. He received the R. W. P. King Prize Paper Award from the IEEE Antennas and Propagation Society for the Best Paper of the Year 2000, by an author under 36. He was the Founder and the EU Coordinator of the EU Doctoral Programs on Metamaterials from 2004 to 2009. From 2002 to 2008, he served as an Associate Editor for the IEEE TRANSACTIONS ON ANTENNAS AND PROPAGATION. He is an Editor of the *Metamaterials Handbook* (Boca Raton, FL, USA: CRC Press, 2009). He is a Fellow of OPTICA.

A. LEE SWINDLEHURST (Fellow, IEEE) received the B.S. and M.S. degrees in electrical engineering from Brigham Young University in 1985 and 1986, respectively, and the Ph.D. degree in electrical engineering from Stanford University in 1991. He was with the Department of Electrical and Computer Engineering, BYU from 1990 to 2007, where he served as the Department Chair from 2003 to 2006. From 1996 to 1997, he held a joint appointment as a Visiting Scholar with Uppsala University and the Royal Institute of Technology, Sweden. From 2006 to 2007, he was on leave working as the Vice President of Research with ArrayComm LLC, San Jose, CA, USA. Since 2007, he has been with the Electrical Engineering and Computer Science Department, University of California at Irvine, where he is a Distinguished Professor and currently serving as the Department Chair. From 2014 to 2017, he was also a Hans Fischer Senior Fellow with the Institute for Advanced Studies, Technical University of Munich. His research focuses on array signal processing for radar, wireless communications, and biomedical applications. He received the 2000 IEEE W. R. G. Baker Prize Paper Award, the 2006 IEEE Communications Society Stephen O. Rice Prize in the Field of Communication Theory, the 2006, 2010, and 2021 IEEE Signal Processing Society's Best Paper Awards, the 2017 IEEE Signal Processing Society Donald G. Fink Overview Paper Award, the Best Paper Award at the 2020 and 2024 IEEE International Conferences on Communications, the 2022 Claude Shannon-Harry Nyquist Technical Achievement Award from the IEEE Signal Processing Society, and the 2024 Fred W. Ellersick Prize from the IEEE Communications Society. In 2016, he was elected as a Foreign Member of the Royal Swedish Academy of Engineering Sciences (IVA).